

Molecular Mechanisms and New Treatment Paradigm for Atrial Fibrillation

Padmini Sirish, PhD; Ning Li, PhD; Valeriy Timofeyev, PhD; Xiao-Dong Zhang, PhD; Lianguo Wang, MD; Jun Yang, PhD; Kin Sing Stephen Lee, PhD; Ahmed Bettaieb, PhD; Sin Mei Ma, BS; Jeong Han Lee, PhD; Demetria Su, BS; Victor C. Lau, BS; Richard E. Myers, PhD; Deborah K. Lieu, PhD; Javier E. López, MD; J. Nilas Young, MD; Ebenezer N. Yamoah, PhD; Fawaz Haj, PhD; Crystal M. Ripplinger, PhD; Bruce D. Hammock, PhD; Nipavan Chiamvimonvat, MD

Background—Atrial fibrillation represents the most common arrhythmia leading to increased morbidity and mortality, yet, current treatment strategies have proven inadequate. Conventional treatment with antiarrhythmic drugs carries a high risk for proarrhythmias. The soluble epoxide hydrolase enzyme catalyzes the hydrolysis of anti-inflammatory epoxy fatty acids, including epoxyeicosatrienoic acids from arachidonic acid to the corresponding proinflammatory diols. Therefore, the goal of the study is to directly test the hypotheses that inhibition of the soluble epoxide hydrolase enzyme can result in an increase in the levels of epoxyeicosatrienoic acids, leading to the attenuation of atrial structural and electric remodeling and the prevention of atrial fibrillation.

Methods and Results—For the first time, we report findings that inhibition of soluble epoxide hydrolase reduces inflammation, oxidative stress, atrial structural, and electric remodeling. Treatment with soluble epoxide hydrolase inhibitor significantly reduces the activation of key inflammatory signaling molecules, including the transcription factor nuclear factor κ -light-chain-enhancer, mitogen-activated protein kinase, and transforming growth factor- β .

Conclusions—This study provides insights into the underlying molecular mechanisms leading to atrial fibrillation by inflammation and represents a paradigm shift from conventional antiarrhythmic drugs, which block downstream events to a novel upstream therapeutic target by counteracting the inflammatory processes in atrial fibrillation.

(*Circ Arrhythm Electrophysiol.* 2016;9:e003721. DOI: 10.1161/CIRCEP.115.003721.)

Key Words: animal model ■ arrhythmia ■ atrial fibrillation ■ eicosanoids ■ inflammation

Atrial fibrillation (AF) represents one of the most common arrhythmias seen clinically and is associated with a significant increase in morbidity and mortality,¹ yet, current treatment paradigms have proven largely inadequate.² Treatment with conventional antiarrhythmic drugs generally carries a high risk of proarrhythmia.³ Moreover, prevalence of AF is increasing because of the aging population.

There is a strong evidence supporting the involvement of inflammation in the pathophysiology of AF.^{1,4,5} Inflammatory infiltrates and increased serum levels of proinflammatory cytokines have been demonstrated in animal models and patients with AF.^{6–8} In addition, inflammation has been implicated in diseases that predispose patients to AF and AF-related processes including oxidative stress and fibrosis.^{5,7} Structural and electric remodeling represent the main pathophysiological

mechanisms contributing to the initiation and maintenance of AF. Moreover, AF can exacerbate inflammation that further perpetuates the arrhythmia. Hence, reduction of inflammation and reversal of structural remodeling have increasingly become the focus of new therapeutic strategies for the treatment of AF.

One of the most robust inflammatory responses is the activation of phospholipase A₂ and the release of arachidonic acid, which is metabolized through the cyclooxygenase, lipoxygenase, and cytochrome P450 pathways. The cytochrome P450 epoxidized products, the epoxyeicosatrienoic acids have been shown to have anti-inflammatory and profibrinolytic with several cardioprotective effects.⁹ However, epoxyeicosatrienoic acids are further metabolized by the soluble epoxide hydrolase (sEH) enzyme to form the corresponding

Received October 27, 2015; accepted April 1, 2016.

From the Division of Cardiovascular Medicine (P.S., N.L., V.T., X.-D.Z., S.M.M., D.S., V.C.L., R.E.M., D.K.L., J.E.L., N.C.), Department of Pharmacology (L.W., C.M.R.), Department of Entomology and Nematology, Comprehensive Cancer Center (J.Y., K.S.S.L., B.D.H.), Department of Nutrition (A.B., F.H.), and Department of Cardiothoracic Surgery (J.N.Y.), University of California, Davis; Department of Physiology and Cell Biology, University of Nevada, Reno (J.H.L., E.N.Y.); and Department of Veterans Affairs, Northern California Health Care System, Mather (N.C.).

The Data Supplement is available at <http://circep.ahajournals.org/lookup/suppl/doi:10.1161/CIRCEP.115.003721/-/DC1>.

Correspondence to Nipavan Chiamvimonvat, MD, Division of Cardiovascular Medicine, University of California, Davis, 451 Health Science Dr, GBSF 6315, Davis, CA 95616. E-mail: nchiamvimonvat@ucdavis.edu

© 2016 American Heart Association, Inc.

Circ Arrhythm Electrophysiol is available at <http://circep.ahajournals.org>

DOI: 10.1161/CIRCEP.115.003721

WHAT IS KNOWN

- Atrial fibrillation (AF) represents the most common arrhythmia leading to increased morbidity and mortality, yet, current treatment strategies have proven inadequate.
- The soluble epoxide hydrolase enzyme (sEH) catalyzes the hydrolysis of anti-inflammatory epoxy fatty acids including epoxyeicosatrienoic acids from arachidonic acid to the corresponding diols.

WHAT THE STUDY ADDS

- Inhibition of sEH reduces inflammation, oxidative stress, fibrosis, and electrical remodeling. Mechanistically, treatment with sEH inhibitor significantly reduces the activation of key inflammatory signaling molecules, including the transcription factor nuclear factor κ -light-chain-enhancer (NF- κ B), mitogen-activated protein kinase (MAPK) and transforming growth factor- β (TGF- β).
- This study provides insights into the underlying molecular mechanisms leading to AF by inflammation and represents a paradigm shift from conventional antiarrhythmic drugs which block downstream events to a novel upstream therapeutic target by counteracting the inflammatory processes in AF.

1,2-diols, dihydroxyeicosatrienoic acids with diminished anti-inflammatory activities.⁹ Indeed, the cardioprotective activity of epoxyeicosatrienoic acids can be enhanced by blocking the degradation of epoxyeicosatrienoic acids to corresponding dihydroxyeicosatrienoic acids using potent inhibitors of sEH (sEHI).¹⁰ We have previously demonstrated the beneficial effects of sEHIs in clinically relevant models of cardiac hypertrophy and failure.^{11–14} We further demonstrate that treatment with sEHIs reduces atrial arrhythmia inducibility in cardiac hypertrophy models.¹² However, the molecular mechanisms underlying the prevention of atrial arrhythmia inducibility by sEHIs remain unexplored.

Hence, in this study, we sought to directly test the molecular mechanisms in the prevention of AF using an in vivo pressure-overload model to replicate chronic hypertension, a major risk factor for AF. We further use an in vitro model of human-induced pluripotent stem cell (hiPSC)-derived atrial myocytes and fibroblasts to test the hypotheses that inhibition of sEH attenuates AF by reducing (1) inflammation, (2) atrial structural remodeling, and (3) electric remodeling in atrial myocytes. Our study not only provides important mechanistic insights into the roles of inflammation and atrial fibrosis in AF but also represents a proof-of-concept study for a novel therapeutic target for the treatment of AF.

Methods

The animal study was performed in accordance with the approved UC Davis Animal Care and Use protocol. Additional experimental details can be found in the Methods in the Data Supplement.

Thoracic Aortic Constriction Model in Mice

Thoracic aortic constrictions (TACs) were performed in 8- to 12-week-old male C57BL/6J mice as previously described.¹³ One week after surgery, mice were randomized in an investigator-blinded manner to receive either vehicle alone or 1-trifluoromethoxyphenyl-3-(1-propionylpiperidine-4-yl)urea (TPPU; Figure 1A) for 3 weeks (Figure 1B).¹³

Analysis of Cardiac Function by Echocardiography

Echocardiograms were performed as described previously.¹² Fractional shortening was calculated from left ventricle dimensions as follows: % fractional shortening = $(\text{end diastolic dimension} - \text{end systolic dimension}) / \text{end diastolic dimension} \times 100$.

Histological Analyses

Excised hearts were retrogradely perfused with phosphate-buffered solution to wash out blood. Fixed hearts were embedded in paraffin, and serial left atrial (LA) and right atrial (RA) sections of 5 μ m in thickness were taken along the longitudinal axis and stained with Picrosirius Red to assess for collagen content.

Immunofluorescence Confocal Laser Scanning Microscopy

Additional cardiac sections were stained with wheat germ agglutinin. Deparaffinized sections were rehydrated with serial dilution of ethanol, serum blocked, and stained. Sections from corresponding area from the 4 groups were scanned.

Flow Cytometric and Electrophysiological Studies of Single Isolated Cardiac Cells

Single cells were obtained using enzymatic digestion. LA and RA myocytes were used for electrophysiological studies using conventional whole-cell patch-clamp technique at room temperature.¹² Currents were recorded using Axopatch 200B amplifier, filtered at 10 kHz, and digitized at sampling frequency of 50 kHz.

For flow cytometric analysis, fixed cells were permeabilized, stained with anti-Thy1.2, lineage, anti-CD45, anti-troponin T, anti-CD31, anti-phosphorylated extracellular signal-regulated kinase 1 and 2 (pERK1/2), anti-phosphorylated Smad2/3 (pSMAD2/3), Ki67 antibodies, and 7-aminoactinomycin D. Data were collected using FACScan cytometer and analyzed using FlowJo software. Cells stained with isotype-matched IgG antibodies were used as controls to determine the positive cell population.

Human-Induced Pluripotent Stem Cell-Derived Cardiomyocytes

HiPSCs were plated and differentiated for 20 days using a directed differentiation protocol.¹⁵ HiPSC-cardiomyocytes (CMs) enriched with puromycin and treated with tumor necrosis factor- α (TNF- α) or angiotensin II (ANG II) and TPPU were fixed and stained with anti- α -actinin, anti-nuclear factor κ -light-chain-enhancer (NF- κ B), anti-myosin light chain-2a (MLC2a), anti-MLC-2v (MLC2v), and fibroblast-specific antibodies.

In Vitro Human Cardiac Fibroblast Culture

Human RA appendage specimens from informed consented patients undergoing cardiac bypass surgery were obtained from UC Davis Medical Center in accordance with the approved UC Davis Institutional Review Board protocol. Partially digested cardiac tissues were plated on cell culture dishes until the appearance of fibroblasts from the explants. Trypsinized cells were replated, treated with ANG II and TPPU and stained with anti-Thy1.1, lineage, anti-CD45, and Ki67 antibodies for flow cytometry.

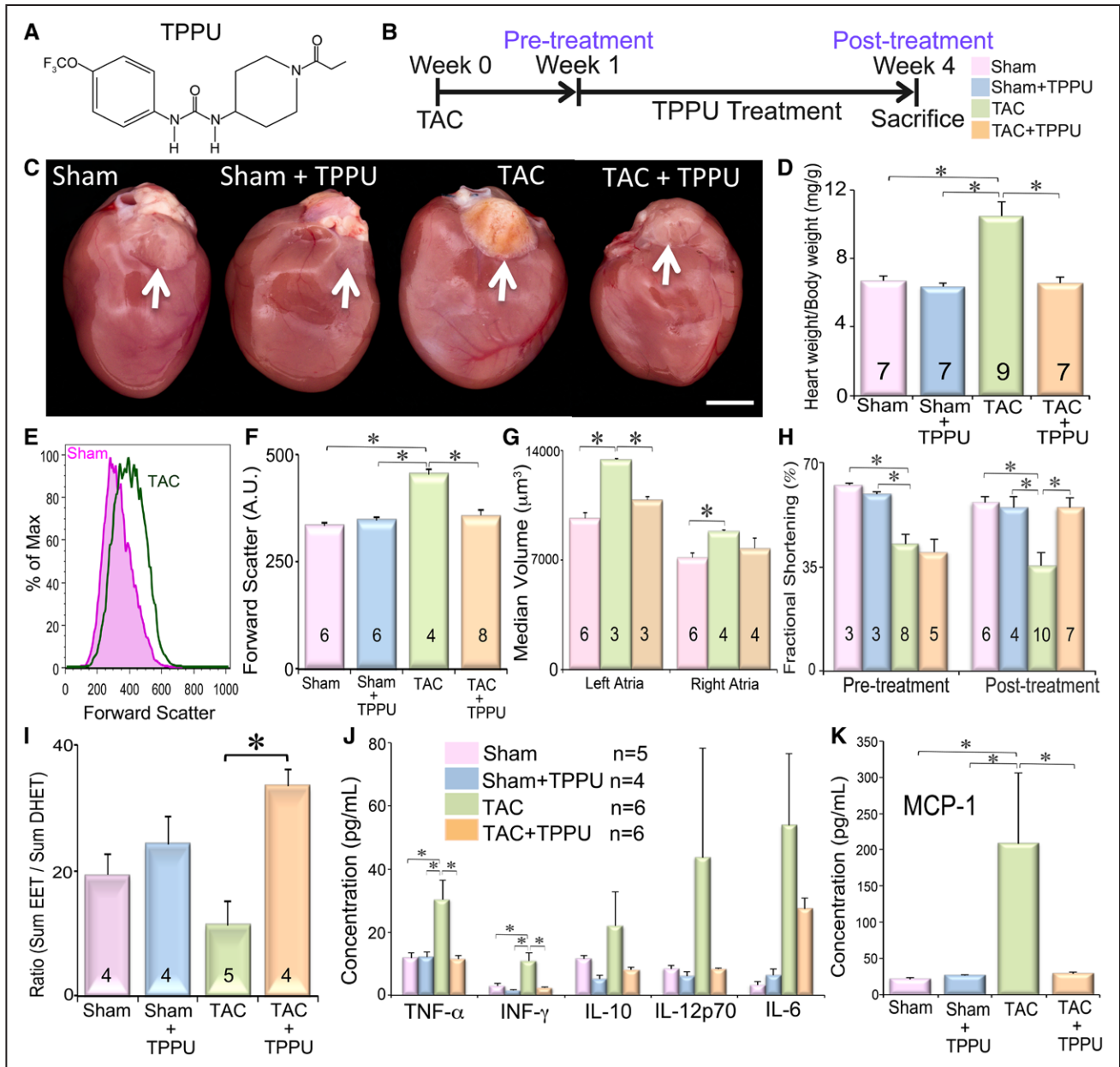


Figure 1. 1-Trifluoromethoxyphenyl-3-(1-propionylpiperidine-4-yl) urea (TPPU) prevents the development of atrial fibrosis in a murine thoracic aortic constriction (TAC) model. **A**, Structure of the inhibitors of soluble epoxide hydrolase enzyme, TPPU used in our studies. **B**, Schematic representation of the experimental protocol. **C**, Examples of whole hearts showing evidence of atrial dilatation in TAC mice. Scale, 1 cm. **D**, Summary data for heart weight/body weight (mg/g). **E**, Flow cytometric analysis of isolated single-nucleated atrial cardiomyocytes (cTnT positive). **F**, Summary data from (e). **G**, Atrial myocyte volume measurements by the Coulter Multisizer assay. **H**, Summary data for % fractional shortening. **I**, Oxylipin profiling at 3 weeks of follow-up. **J**, Serum concentration of cytokines and chemokine (**K**). Scale bars, 20 μ m. Mean \pm SEM, Numbers inside the graph represents n. DHET indicates dihydroxyeicosatrienoic acid; EET, epoxyeicosatrienoic acid; IL, interleukin; INF, interferon; MCP, monocyte chemoattractant protein; and TNF, tumor necrosis factor. * P <0.05.

Western Blot Analysis

Immunoblots were performed as previously described¹⁶ using anti-I κ B, antiphospho-I κ B, anti-NF- κ B, and anti-GAPDH antibodies.

Measurement of Plasma Cytokine Levels

Plasma cytokine levels from samples collected 3 weeks after sham or TAC operations were analyzed using a Cytometric Bead Array kit and Cytometric Bead Array Analysis software following the manufacturer's protocol.¹³

Evaluation of Endoplasmic Reticulum Stress markers

Total protein isolated from atrial tissues homogenized in radio-immunoprecipitation assay (RIPA) buffer supplemented with protease and phosphatase inhibitors were resolved by SDS-PAGE, and immunoblotting was performed using antibodies for pp38 (Thr180/Tyr182), p38, pJNK (Thr183/Tyr185), c-Jun N-terminal kinases (JNK), pPERK (Thr980), PERK, pEIF2 α (Ser51), eukaryotic translation initiation factor 2 (eIF2 α), sXBP1, inositol requiring enzyme 1 α (IRE1 α), pIRE1 α (Ser724), and tubulin. Proteins were visualized

using enhanced chemiluminescence and quantified using ImageQuant 5.0 software. Data for phosphorylated proteins are presented as phosphorylation level normalized to total protein expression and for non-phosphorylated proteins as total protein expression normalized to β -tubulin.

Ex Vivo Optical Mapping of Transmembrane Potential (V_m)

Hearts from heparin-injected anesthetized mice were perfused in Tyrode solution with the posterior surface of the heart facing the optical mapping camera using Langendorff apparatus.¹⁷ A bipolar pacing electrode was positioned on the epicardium of LA or RA appendage for pacing using a 2 ms pulse at twice the diastolic threshold. The heart was stained with the voltage-sensitive dye (RH237) via the coronary perfusion. Optical action potentials were recorded using a 16-bit complementary metal oxide camera and images acquired at 1 kHz.

Statistical Analysis

Statistical comparisons were analyzed by 1-way ANOVA followed by Bonferroni tests and Tukey–Kramer honest significant difference analyses for post hoc comparison.

Results

Prevention of Atrial Myocyte Hypertrophy With sEH in a Murine TAC Model

TPPU has been shown previously to have high inhibitory potency, long enzyme dissociation half-life, pharmacokinetic half-life with drug-like properties, and a comparable elevation of epoxyeicosatrienoic acids concentration in plasma as the sEH knockout mice (*EPHX2*^{-/-}).^{13,18} TAC mice exhibited cardiac hypertrophy, a significant increase in heart weight/body weight ratio (HW/BW; Figure 1C and 1D) and atrial dilation (Figure 1A and 1B in the Data Supplement). In contrast, treatment with TPPU in TAC mice resulted in a decrease in HW/BW ratio and atrial dilatation. Flow cytometry confirmed the presence of the sEH enzyme in the atrial myocytes (Figure 1C in the Data Supplement).

We analyzed the forward light scattering by flow cytometry as an index of atrial myocyte size using isolated single atrial cells. Atrial myocytes were gated based on the presence of cardiac-specific troponin T. There was a significant increase in atrial myocyte size in TAC-operated group (Figure 1E and 1F) compared with sham-operated groups. More importantly, atrial myocyte hypertrophy was reduced in animals treated with TPPU (Figure 1F). We further confirmed the findings using patch-clamp recordings and cell capacitance measurement showing a significant increase in myocyte size in TAC-operated mice (118±4 pF) compared with sham, sham-operated, and TAC–TPPU treated groups (64±10, 67±7, and 71±2 pF, respectively). Finally, the myocyte size from LA and RA was directly compared using a Coulter multisizer assay to quantify the cell volume.¹³ The myocyte volume significantly increased in both LA and RA from TAC mice, which was restored to the sham-operated control levels by the TPPU treatment (Figure 1G). Interestingly, the myocyte volume was significantly smaller for RA compared with LA in all 3 groups (sham, TAC, and TAC-treated; $P < 0.05$).

The effect of TPPU on the chamber size and systolic function was assessed using echocardiography. There was a significant decrease in left ventricular end-diastolic dimension

(Figure II in the Data Supplement) associated with a significant improvement in fractional shortening (Figure 1H) post TPPU treatment. In contrast, left ventricular end-diastolic dimension in TAC mice increased from week 1 to week 4 suggesting adverse remodeling.

Target Engagement of TPPU in Mouse TAC Model

To demonstrate the inhibition of sEH by TPPU, metabolic profiling of arachidonic acid metabolites of the cytochrome P450 pathway was performed after 3 weeks of treatment as previously described.¹³ There was a significant increase in the epoxyeicosatrienoic acids/dihydroxyeicosatrienoic acids ratio in the TPPU-treated groups compared with TAC alone group (Figure 1I; Table I in the Data Supplement). Moreover, analysis of arachidonic acid metabolites of the cyclooxygenase pathway demonstrates an increase in proinflammatory thromboxane and prostaglandin levels in the TAC model, which was attenuated with TPPU treatment (Figure IIIA and Table II in the Data Supplement). Metabolites of the lipoxygenase pathways demonstrated a modest difference between the 4 groups (Figure IIIB and Table II in the Data Supplement).

Treatment With TPPU Results in a Significant Reduction in Inflammatory Cytokines and Chemokine

Although the precise underlying mechanisms for atrial fibrosis in AF have not been fully elucidated, a network of profibrotic factors including proinflammatory cytokines is known to contribute toward AF in the clinical setting.¹⁹ Our data demonstrate a significant increase in proinflammatory cytokine and chemokine levels including interferon- γ , TNF- α , and monocyte chemoattractant protein-1 in the TAC mice (Figure 1J and 1K). Importantly, treatment with TPPU significantly decreased the cytokine and chemokine levels.

Treatment With TPPU Significantly Reduces Atrial Fibrosis and Atrial Fibroblast Activation

Previous studies have provided a strong link between atrial fibrosis and atrial structural remodeling in the development of AF^{1,4}; however, the precise mechanisms for atrial fibrosis remain incompletely understood. The secretory, migratory, and proliferative capacity of cardiac fibroblasts increases after injury.¹³ Proinflammatory cytokines and profibrotic factors, such as ANG II, induce cardiac fibrosis by activating cardiac fibroblasts resulting in an increase in collagen synthesis.¹ However, there are regional differences in structural remodeling between atria and ventricles with atria being particularly prone to fibrosis.²⁰ Indeed, atrial fibroblasts are distinct from ventricular fibroblasts in their morphology, gene expression, secretory, and proliferative patterns.²¹

Here, we demonstrate the presence of atrial fibrosis in LA (Figure 2A and 2B) and RA (Figure IV in the Data Supplement) sections using Picrosirius Red stain and wheat germ agglutinin that binds to highly glycosylated collagen protein in TAC hearts. However, there was a marked decrease in collagen deposition in the TPPU-treated atrial tissue sections compared with the TAC alone. Next, we analyzed atrial fibroblasts isolated from sham, sham-treated, TAC, and

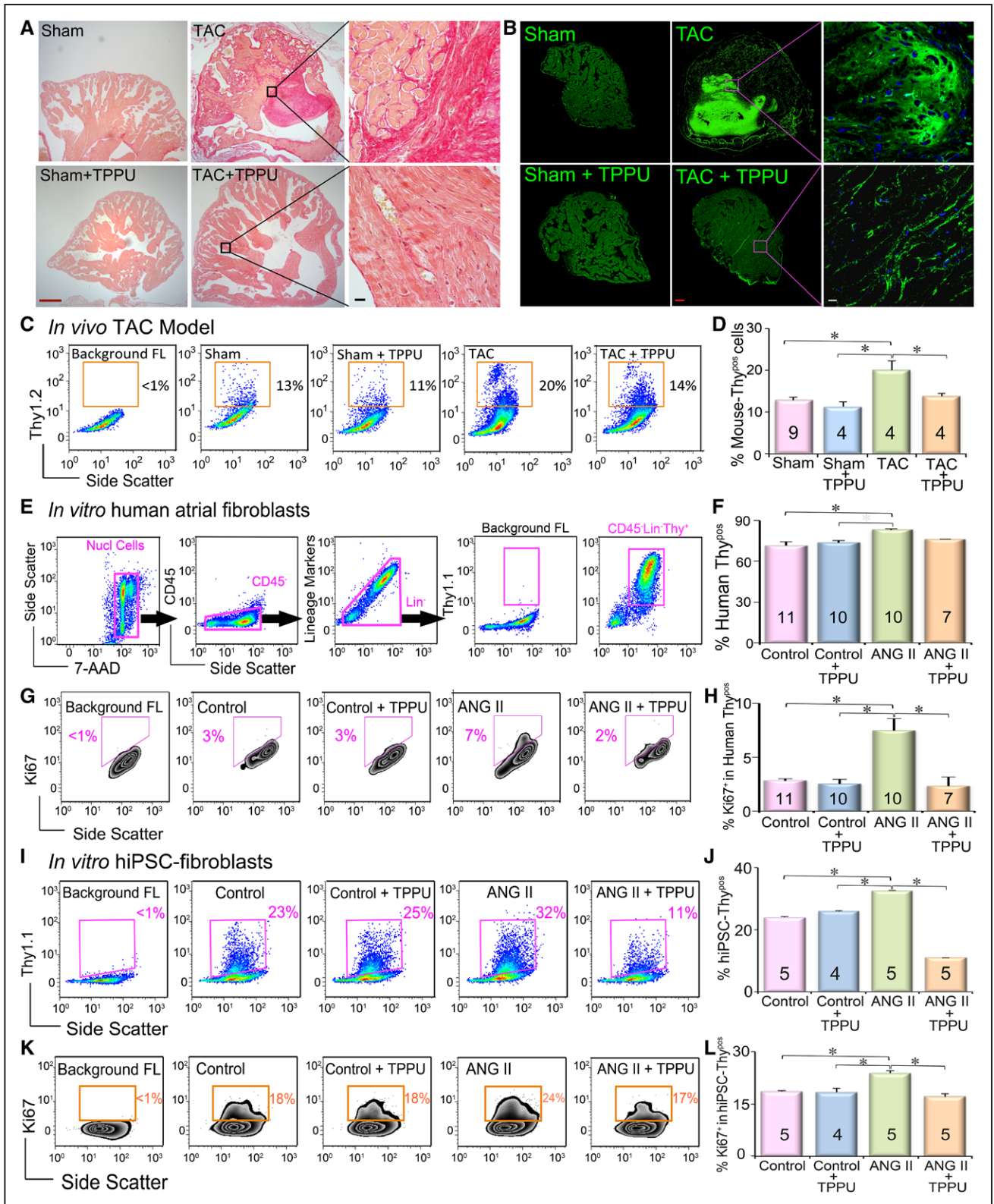


Figure 2. 1-Trifluoromethoxyphenyl-3-(1-propionylpiperidine-4-yl) urea (TPPU) reduces atrial fibrosis and atrial fibroblast activation. **A**, Cardiac sections stained with Sirius Red demonstrate the amount of collagen deposition. Scale bars; red, 500 μ m and black, 20 μ m. **B**, Confocal images of wheat germ agglutinin stain showing a significant decrease in collagen deposition in the TPPU-treated thoracic aortic constriction (TAC) mice compared with TAC alone. Scale bars; red, 200 μ m and white, 20 μ m. **C**, Flow cytometric analysis of Thy1.2⁺/Lin⁻/CD31⁻/CD45⁻/CD34⁻ (Thy^{pos}) cells. x and y axes represent arbitrary units. **D**, Summary data from **C**. **E**, Nucleated cells were enumerated based on the incorporation of 7-aminoactinomycin D from human atrial fibroblasts derived from human atrial appendage specimens from patients undergoing cardiac bypass surgery. Human atrial fibroblasts were identified as Thy1.1⁺/CD45⁻/Lin⁻ (Human-Thy^{pos}) cells. **F**, Flow cytometric analysis of human-Thy^{pos} cells. **G**, Flow cytometric analysis of the proliferation of human-Thy^{pos} using Ki67. **H**, (Continued)

Figure 2 Continued. Summary data from **G, I**, Flow cytometric analysis of Thy1.1⁺/CD45⁻/Lin⁻ (hiPSC-Thy^{pos}) cells derived from human-induced pluripotent stem cells (hiPSCs). **J**, Summary data from **I, K**, Flow cytometric analysis of the proliferation of hiPSC-Thy^{pos} cells using Ki67. **L**, Summary data from **K**. Representative results are shown. Mean±SEM. Numbers inside the graph represents n. ANG II indicates angiotensin II; and FL, fluorescence. **P*<0.05.

TAC-treated hearts. Atrial fibroblasts were defined as Thy1.2⁺/Lin⁻/CD31⁻/CD45⁻ cells (Mouse-Thy^{pos} cells) using flow cytometry.¹³ There was a significant increase in percentages of Thy^{pos} cells in the atria of TAC compared with the 2 groups of sham animals (Figure 2C and 2D). Treatment with TPPU resulted in a significant decrease in percentages of Thy^{pos} cells compared with TAC animals.

In Vitro Models of Human Atrial Fibroblasts and hiPSC-Derived Cardiac Fibroblasts

The effects of TPPU observed in the atria may be secondary to the reduction in ventricular hypertrophy and adverse remodeling in the ventricles. Therefore, to directly demonstrate the effects of sEH inhibition specifically on atrial fibroblasts and independent of ventricular influence, we used atrial fibroblasts isolated from human atrial appendages as well as an in vitro model of hiPSC-derived cardiac fibroblasts (hiPSC-fibroblasts).

Human atrial fibroblasts were isolated and quantified as cells expressing Thy1.1⁺/Lin⁻/CD45⁻ (Human-Thy^{pos} cells) using flow cytometry (Figure 2E). There was a significant increase in percentages of human atrial fibroblasts in the ANG II-treated group compared with the control (Figure 2F), and treatment with TPPU resulted in a decrease in percentages of human Thy^{pos} cells. We further used Ki67 to analyze the proliferative capacity among human atrial fibroblasts stimulated with ANG II. There was a significant increase in the percentage of Ki67 in the ANG II-treated human atrial fibroblasts compared with control (Figure 2G and 2H). Treatment with TPPU in the ANG II-stimulated cells resulted in a significant decrease in Ki67 expression in human atria fibroblasts.

HiPSC-fibroblasts were defined as Thy1.1⁺/Lin⁻/CD45⁻ cells (hiPSC-Thy^{pos} cells). ANG II treatment significantly increased the percentages (Figure 2I and 2J) and proliferative capacity (Figure 2K and 2L) of hiPSC-fibroblasts compared with the control. Treatment with TPPU in the ANG II-stimulated cells resulted in a significant decrease in the percentages and Ki67 positivity in the hiPSC-fibroblasts.

Treatment With TPPU Results in a Significant Reduction in the Activation of Mitogen-Activated Protein Kinase and Transforming Growth Factor- β Signaling Cascades in Atrial Fibroblasts and Myocytes

Inflammatory cytokines and chemokines including interferon- γ , TNF- α , and monocyte chemoattractant protein-1 have been shown to contribute to cardiac fibrosis by activating cardiac fibroblasts via the mitogen-activated protein kinase (MAPK) signaling cascade.¹³ Indeed, increased circulatory levels of TNF- α have been demonstrated in patients with heart failure.²² The Smad signaling cascade regulated by transforming growth factor- β (TGF- β) also contributes to cardiac fibrosis.²³ Upregulated TGF- β in cardiac fibroblasts activates Smad

transcription factors, which translocate to the nucleus to activate the promoters of collagen I and III genes.^{24,25} Moreover, cardiac hypertrophy is also stimulated by the interplay of MAPK and TGF- β .^{25,26}

To elucidate the effects of TPPU on the MAPK and TGF- β signaling cascades, we examined the activation of downstream members, the ERK1/2 and Smad2/3 in atrial fibroblasts and myocytes. Our data demonstrate a significant elevation in the levels of phosphorylated ERK1/2 (pERK1/2) in atrial fibroblasts (Figure 3A and 3B) and myocytes (Figure 3C and 3D) in the TAC mice that was significantly decreased in TPPU-treated TAC mice. Similarly, there was a significant elevation in the levels of pSmad2/3 in atrial fibroblasts (Figure 3E and 3F) and myocytes (Figure 3G and 3H) in the TAC mice that was significantly decreased in TPPU-treated TAC mice. Taken together, our data suggest that TPPU decreases the production of cytokines and chemokines resulting in the decrease in the activation of atrial fibroblasts and myocyte hypertrophy, the leading contributors of adverse atrial structural remodeling associated with AF.

Treatment With TPPU Results in a Significant Reduction in Oxidative Stress in Atrial Fibroblasts and Myocytes

Systemic and myocardial-specific oxidative stress has been implicated in the pathogenesis of AF.²⁷ Elevated systemic levels of reactive oxygen species (ROS) are seen with increasing age, heart failure, and coronary heart disease, which are known risk factors for AF.²⁸ Here, flow cytometry was used to quantify the level of oxidative stress in atrial fibroblasts (Figure 3I and 3J) and atrial myocytes (Figure 3K and 3L). There was a significant increase in ROS levels in atrial fibroblasts and atrial myocytes isolated from TAC compared with the 2 groups of sham animals. Moreover, treatment with TPPU resulted in a significant decrease in the ROS activity compared with TAC alone.

Direct Effects of TPPU in an In Vitro Model of hiPSC-Derived Atrial Myocytes and Fibroblasts Activated by Inflammatory Cytokine TNF- α

As mentioned above, the effects of sEH in the prevention of atrial remodeling may be secondary to the reduction in ventricular hypertrophy. Therefore, to specifically elucidate the effects of inflammatory cytokines and the direct inhibitory effects of TPPU on atria, we used an in vitro model of hiPSC-derived atrial myocytes (hiPSC-ACMs) and hiPSC-fibroblasts. HiPSC-ACMs were selected based on the expression of MLC2a and the absence of MLC2v (Figure 4A and 4B).²⁹ Differentiated-hiPSCs were treated with TNF- α . Analysis of hiPSC-ACMs (MLC2a⁺/MLC2v⁻) and hiPSC-fibroblasts stimulated with TNF- α demonstrated a significant increase in pERK1/2 compared with the control and control-TPPU-treated cells (Figure 4C through 4E). Moreover, treatment of TNF- α stimulated hiPSC-ACMs and hiPSC-fibroblasts with TPPU significantly decreased the pERK1/2 level. The presence of the sEH enzyme in hiPSCs was analyzed by flow cytometry (Figure 4F).

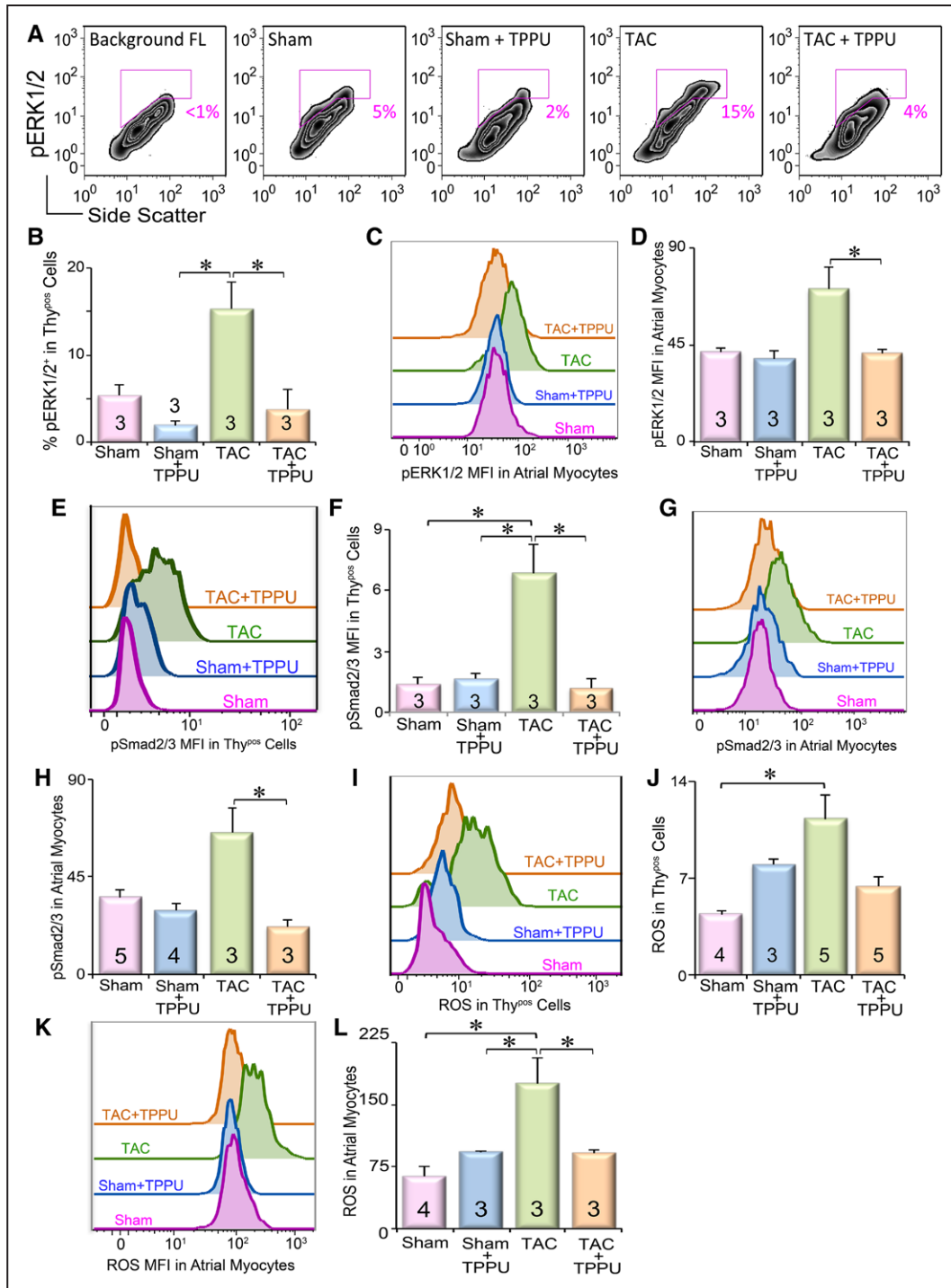


Figure 3. Flow cytometric analysis of the activation of atrial cardiac fibroblasts and atrial myocytes in the in vivo thoracic aortic constriction (TAC) model. **A**, Flow cytometric analysis of pERK1/2⁺ of atrial fibroblasts. **B**, Summary data from **A**. **C**, Flow cytometric analysis showing the median fluorescence intensity of pERK1/2⁺ of atrial myocytes. **D**, Summary data from **C**. **E**, Flow cytometric analysis of pSmad2/3⁺ in atrial fibroblasts. **F**, Summary data from **E**. **G**, Flow cytometric analysis of pSmad2/3⁺ of atrial myocytes. **H**, Summary data from **G**. **I**, Flow cytometric analysis of reactive oxygen species (ROS) of atrial fibroblasts. **J**, Summary data from **I**. **K**, Flow cytometric analysis of ROS of atrial myocytes. **L**, Summary data from **K**. Representative results are shown. Mean±SEM. Numbers inside the graph represent n. *P<0.05.

Treatment With TPPU Results in a Significant Reduction in the Activation of the NF-κB

NF-κB represents one of the critical players in the cytokine-mediated inflammation and is associated with cardiac fibrosis, hypertrophy, and heart failure.⁹ NF-κB is maintained in the

inactive form when bound to IκB. Degradation of IκB by IκB kinase leads to the nuclear translocation of NF-κB and gene activation. Epoxyeicosatrienoic acids have been shown to regulate the NF-κB cascade by inhibiting IκB kinase.⁹ Our data demonstrated an increased nuclear translocation of NF-κB

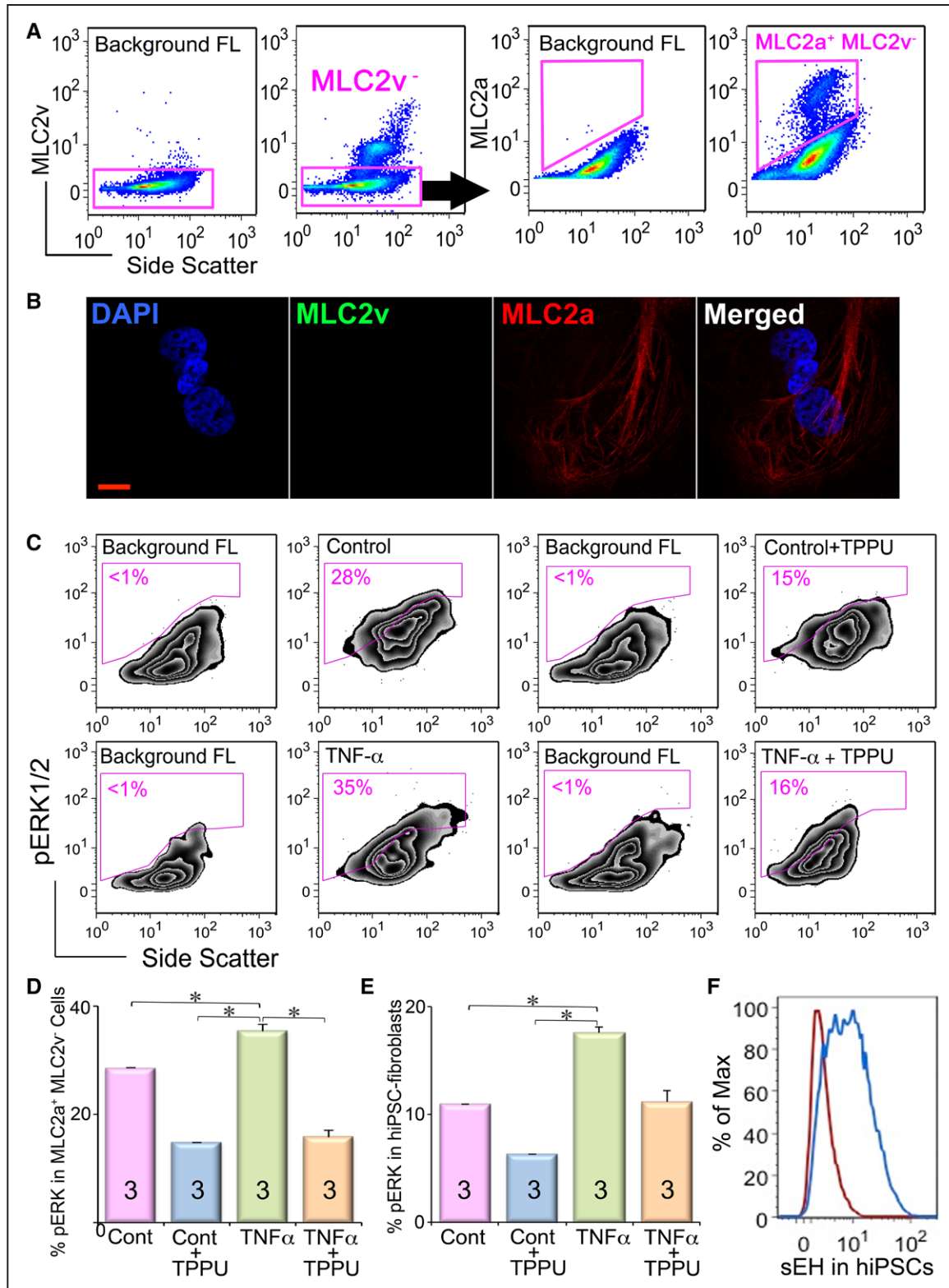


Figure 4. Treatment with 1-trifluoromethoxyphenyl-3-(1-propionylpiperidine-4-yl) urea (TPPU) results in a significant reduction in extracellular signal-regulated kinase 1 and 2 (ERK1/2) in atrial myocytes and fibroblasts in vitro. **A**, Flow cytometric analysis of anti-myosin light chain-2a (MLC2a)⁺ anti-MLC-2v (MLC2v)⁻ cells from human-induced pluripotent stem cells (hiPSC)-derived cardiomyocytes. x and y axes represent arbitrary units. **B**, Immunofluorescence confocal images of MLC2a⁺MLC2v⁻ cells. **C**, Flow cytometric analysis of pERK1/2 signal in MLC2a⁺MLC2v⁻ atrial myocytes treated with tumor necrosis factor- α (TNF- α) alone and with TPPU. **D**, Summary data from **C**. **E**, Flow cytometric summary data showing pERK1/2 signal in hiPSC-fibroblasts (Thy1.1⁺/CD45⁻/Lin⁻) treated with TNF- α alone and with TPPU. **F**, Presence of soluble epoxide hydrolase enzyme in hiPSCs analyzed through flow cytometry. Scale bar, 200 μ mol/L. Mean \pm SEM. Numbers inside the graph represent n. * P <0.05.

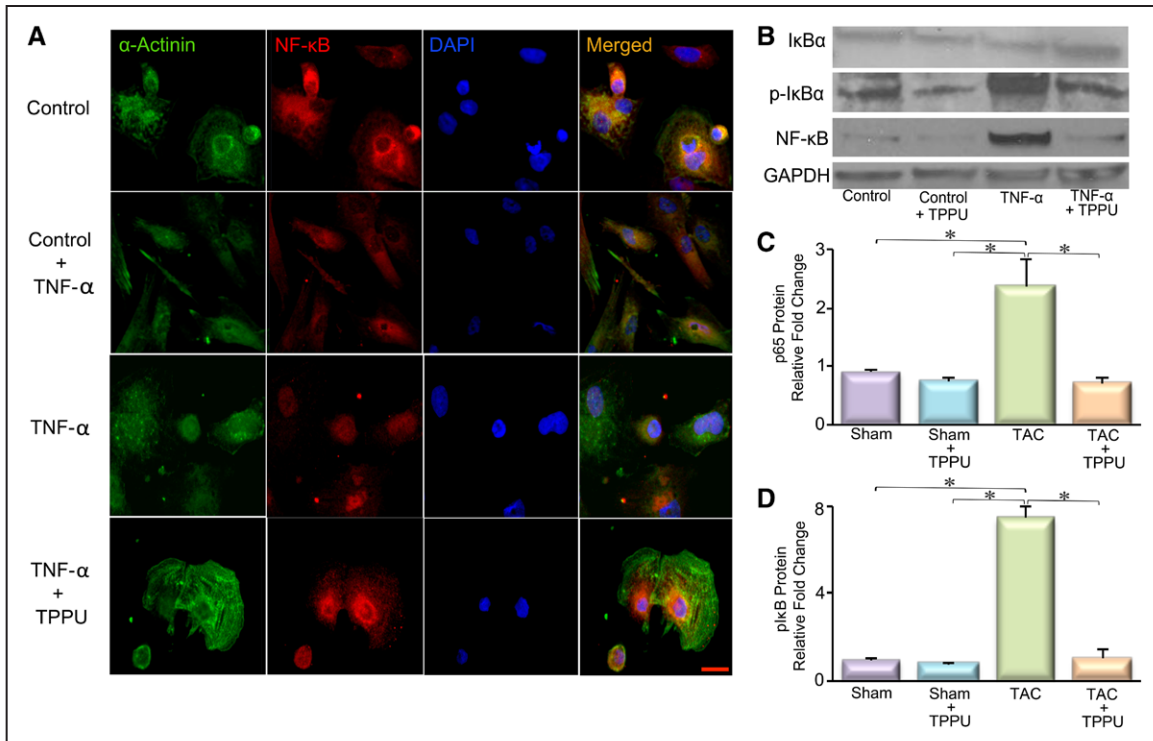


Figure 5. Treatment with 1-(3-(trifluoromethoxy)phenyl)-3-(1-propionylpiperidine-4-yl) urea (TPPU) results in nuclear factor κ B (NF- κ B) activation in human-induced pluripotent stem cell-derived cardiomyocytes (hiPSC-CMs) in vitro. **A**, Prevention of translocation of NF- κ B after treatment with TPPU in cultured hiPSC-CMs stimulated with tumor necrosis factor- α (TNF- α). **B**, Western blot analysis of total I κ B α , phosphorylated I κ B α (pI κ B α), nuclear NF- κ B (nNF- κ B), and GAPDH levels. **C**, Quantification of nuclear NF- κ B and **(D)** pI κ B α normalized to GAPDH. Mean \pm SEM. $n=3$. * $P<0.05$.

in hiPSC-CM (Figure 5A) and a significant increase in the pI κ B α and nuclear NF- κ B (nNF- κ B) on TNF- α stimulation, which was significantly attenuated with TPPU treatment (Figure 5B through 5D).

Treatment With TPPU Results in a Significant Reduction in Endoplasmic Reticulum Stress

Increasing evidence suggests that endoplasmic reticulum (ER) stress contributes to cardiac hypertrophy, fibrosis, and apoptosis.^{30,31} Perturbations in the ER homeostasis because of intrinsic and extrinsic factors, such as inflammation, oxidative stress, and ischemia may culminate in ER stress. This includes the activation of ER transmembrane protein sensors (PKR-like ER-regulated kinase [PERK] and inositol requiring enzyme 1 α [IRE1 α]), the upregulation of ER chaperones, such as binding of immunoglobulin protein, initiation of ER-related apoptotic proteins, such as CCAAT/enhancer-binding protein homologous protein, and activation of MAPKs.³²⁻³⁴

Chronic pressure overload in TAC animals resulted in the activation of PERK and IRE1 α , and their downstream targets α -subunit of eIF2 α and X-box binding protein 1 (XBPI), respectively in atrial tissues (Figure VA in the Data Supplement). Treatment with TPPU significantly attenuated ER stress in atrial tissues as evidenced by decreased PERK (Thr980), eIF2 α (Ser51), and IRE1 α (Ser724) phosphorylation, decreased XBPI splicing expression, and a decrease in binding of immunoglobulin protein and CCAAT/enhancer-binding protein homologous protein compared with TAC mice

(Figure VB through VG in the Data Supplement). Because the activation of MAPKs constitutes a component of the stress response in atrial hypertrophy³⁵ and plays an important role in mediating signal transduction from the ER to the cell nucleus, we evaluated activation of MAPKs. Notably, TAC-induced phosphorylation of p38 (Thr180/Tyr182) and JNK (Thr183/Tyr185) was lower in TPPU-treated TAC mice (Figure VH and VI in the Data Supplement). The β -tubulin levels remain unchanged in the 4 groups (Figure VJ in the Data Supplement).

Treatment With TPPU Reduces Atrial Electric Remodeling

Finally, optical mapping of transmembrane potential (V_m) was performed on isolated atria to determine the effects of TPPU on atrial electric remodeling.³⁶ There was an increase in action potential duration (APD; Figure 6A through 6D) in the atria isolated from TAC compared with TPPU-treated TAC animals. Atria from TAC hearts demonstrated a significant increase in APD at 80% of repolarization (APD₈₀) and APD dispersion (differences between LA and RA APD) compared with the TPPU-treated atria. Furthermore, atria isolated from TAC mice showed significantly longer effective refractory period in the LA versus RA (Figure 6E), indicating increased dispersion of repolarization and refractoriness in untreated hearts.

Consistent with the ex vivo findings, patch-clamp recordings from single isolated atrial myocytes demonstrated a significant downregulation of the transient outward K⁺ current in TAC animals compared with sham or sham-treated animals.

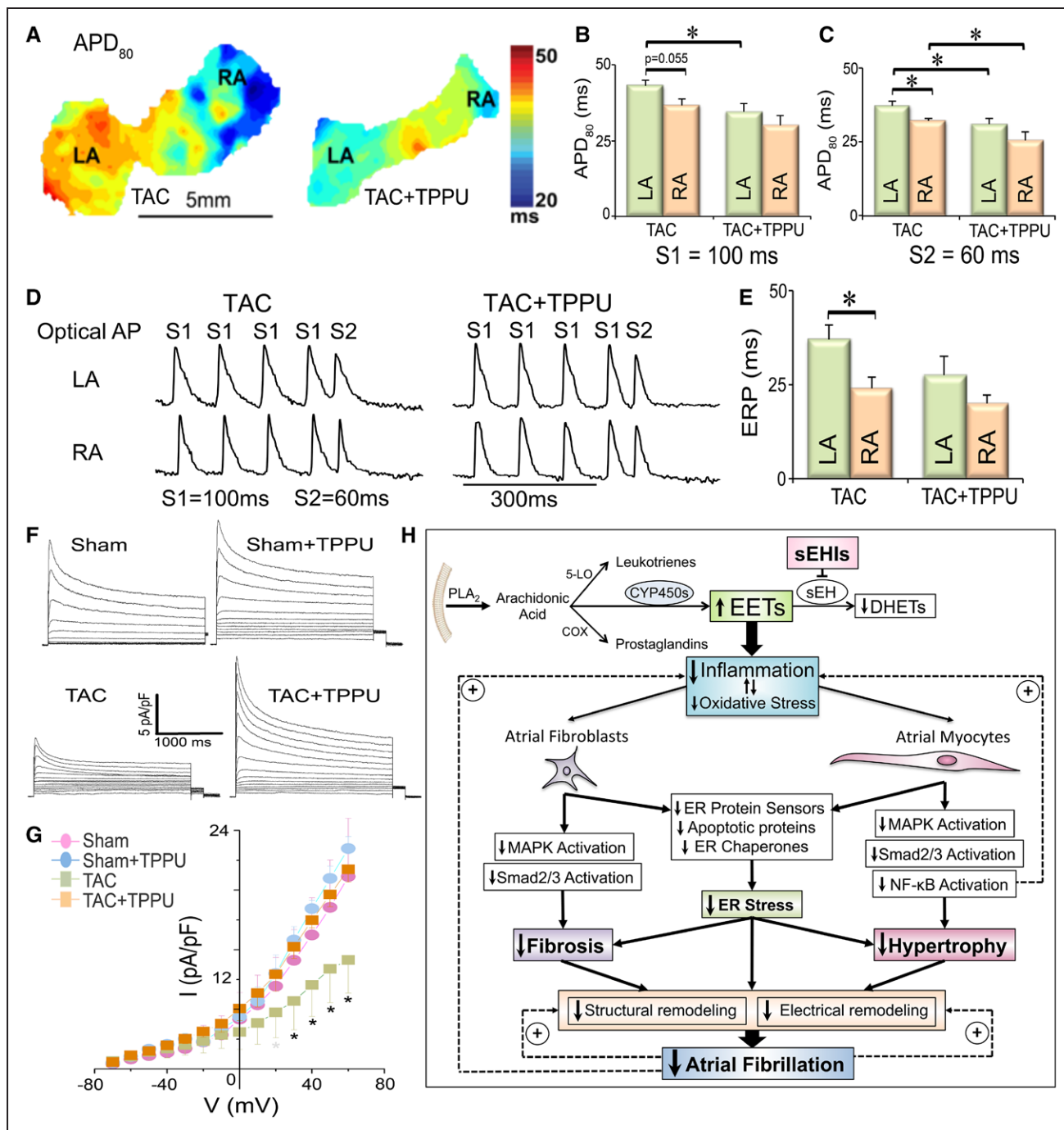


Figure 6. Effect of 1-trifluoromethoxyphenyl-3-(1-propionylpiperidine-4-yl) urea (TPPU) on thoracic aortic constriction (TAC)-induced atrial electrophysiological remodeling: **A**, Example maps of atrial action potential duration (APD) in the untreated (left) and TPPU-treated (right) heart. **B**, Mean APD₈₀ during pacing at a constant cycle length (S1=100 ms). **C**, Mean APD₈₀ during a premature pacing stimulus (S2=60 ms). **D**, Example optical AP traces during S1 (100 ms)-S2 (60 ms) pacing. **E**, Effective refractory period (ERP) measured from both the left atrial (LA) and the right atrial (RA) in untreated and TPPU-treated hearts; n=5 in TAC, n=4 in TAC+TPPU. **F**, Transient outward K⁺ current recordings from single isolated atrial myocytes and **G**) the corresponding current-voltage (I-V) plot. Representative results are shown. **H**, Summary of the various processes involved in the prevention of atrial fibrillation with TPPU treatment. Mean±SEM, n=14. DHET indicates dihydroyeicosatrienoic acids; EET, epoxyeicosatrienoic acid; and MAPK, mitogen-activated protein kinase. *P<0.05.

Treatment with TPPU prevented the downregulation of the transient outward K⁺ current (Figure 6F and 6G).

Discussion

Chronic hypertension represents one of most common comorbidities leading to AF.³⁷ The main pathophysiological

mechanisms contributing to the initiation, progression, and persistence of AF are structural and electric remodeling of the atria.³⁷ Moreover, AF increases inflammation in the heart contributing to atrial remodeling substantiating the AF begets AF phenomenon.⁷ In this study, we provide a proof-of-concept and the molecular mechanisms underlying the beneficial

effects of inhibition of sEH in the treatment of AF. We demonstrate positive effects of sEHI in a pressure-overload-induced atrial remodeling model by reducing (1) inflammation, (2) atrial fibrosis, and (3) electric remodeling in atrial myocytes. Specifically, this study provides evidence to support the role of inhibition of sEH as a potent anti-inflammatory mechanism leading to a significant decrease in the systemic levels of cytokines and chemokines as well as the inhibition of NF- κ B activation. Moreover, treatment with sEHI results in significant attenuation in the phosphorylation of key signaling molecules, including ERK1/2 in the MAPK pathway in atrial myocytes and atrial fibroblasts. To further demonstrate direct inhibitory effects of sEHI on atrial myocytes and atrial fibroblasts, we took advantage of in vitro models of hiPSC-ACMs and hiPSC-fibroblasts as well as human atrial fibroblasts isolated from atrial appendages. Taken together, our data provide compelling molecular and cellular evidence for the use of sEHI as an anti-inflammatory therapy for AF (Figure 6H).

Roles of Inflammation in AF

Inflammation has been shown to play critical roles in the pathophysiology of AF.⁸ Evidence of inflammatory infiltrates and increased serum levels of proinflammatory cytokines were present in both animal models and patients with AF.⁶⁻⁸ Several important molecular mediators in inflammatory responses in AF include the stretch-activated production of ANG II and the recruitment of inflammatory cells that secrete inflammatory cytokines and chemokines that activate one of the critical transcription factors, NF- κ B. Activated NF- κ B not only increases the gene expression of inflammatory cytokines, intensifying inflammation, it also leads to electric remodeling and myocytes hypertrophy. Hence, inflammatory cytokines act via a positive feedback mechanism further exacerbating AF (Figure 6H).

Inflammatory cytokines such as TNF- α and interferon- γ also disrupt protein folding in the ER. The ER is a multifunctional organelle playing an important role in protein-folding, calcium homeostasis, and in particularly in the heart it also contributes to the regulation of excitation-contraction coupling.^{32,34} When the folding capacity of ER is exceeded, misfolded proteins accumulate triggering ER stress. To mitigate ER stress and to restore ER homeostasis, the unfolded protein response is initiated. However, if unfolded protein response mechanisms are unable to lessen ER stress, cardiomyocyte apoptosis occurs that contributes to the development and maintenance of AF.³⁸ In addition, ER stress-induced apoptosis is initiated via the activation of NF- κ B.³⁴ Our data demonstrate a significant attenuation in the ER stress proteins with TPPU treatment. The in vitro data also demonstrate a decrease in the activation of NF- κ B with TPPU treatment. Taken together, our data suggest that treatment with TPPU decreases ER stress at least, in part, through the inhibition of NF- κ B activation.

Atrial Structural Remodeling and AF

AF-induced structural remodeling is a gradual process that intensifies progressively. Excessive oxidative stress has been associated with AF leading to atrial structural remodeling, including atrial myocyte hypertrophy and fibrosis.^{27,28}

Experimental animal models and clinical studies have implicated multifactorial processes including atrial dilatation, cellular hypertrophy, apoptosis, ER stress, fibrosis, and oxidative stress as contributing to structural remodeling.^{27,30} Increased fibrosis initiated by profibrotic cytokines such as TGF- β 1 has been observed in patients with AF.^{1,4,21} Atrial fibrosis has been shown to involve a complex interplay of profibrotic molecules, including ANG II and its downstream mediators, the multifunctional MAPKs, and TGF- β .^{13,24,25} Upregulated TGF- β in cardiac fibroblasts induces cardiac fibrosis by activating Smad transcription factors, which activate the promoters of collagen I and III genes.^{24,25} TGF- β also promotes persistent perivascular and interstitial fibrosis by suppressing the activity of matrix metalloproteinases and protease inhibitors.^{13,25}

Atrial myocyte hypertrophy further increases ROS production in the atrial myocytes resulting in the activation of programmed cell death and apoptosis. Increased ROS production in cardiomyocytes causes the activation of members of the MAPK pathway, ERK1/2 and JNKs, both of which have been implicated in cardiac hypertrophy.³⁹ Similarly, members of the pleiotropic TGF- β superfamily have been shown to promote myocardial hypertrophy.^{25,26}

Here, we demonstrate an increase in both atrial fibrosis and atrial myocyte hypertrophy in the chronic pressure-overload model, which is significantly mitigated by treatment with sEHIs. Treatment with sEHI significantly decreases the activation of ERK1/2 and Smad2/3 in atrial fibroblasts and myocytes. Inhibition of sEH attenuates ROS in atrial myocytes and fibroblasts by preventing the activation of the MAPK pathway, ERK1/2 and JNK. Moreover, sEHI decreases ER stress consistent with previous findings of the reduction of ER stress response in various disease models by sEH inhibition.^{32,33} Finally, direct effects of sEHI on atrial myocytes and fibroblasts are further substantiated using in vitro model of hiPSC-fibroblasts and hiPSC-ACMs.

Atrial Electric Remodeling and AF

Electric remodeling is induced by rapid atrial rates, which develops immediately after AF and contributes to the stability of a longer lasting form of AF. Abnormalities in electric impulse formation or impulse conduction can initiate and maintain AF. Excessive prolongation of APD causes Ca²⁺ currents to recover from inactivation, leading to early after depolarization and maintenance of AF.⁴⁰ Our study demonstrates a slowing of activation, a prolonged APD in LA, and importantly an increased dispersion of APD and effective refractory period, a known proarrhythmic factor. At the cellular basis, electric remodeling involves changes to the ion channels governing the AP characteristics. Downregulation of I_{to} in atrial cells can significantly alter AP shape and duration contributing to electric remodeling. A marked decrease in I_{to} was previously documented in both animal models and patients with chronic AF.⁴¹ The reduction in I_{to} has been shown to be because of the decrease in the auxiliary subunit of the K⁺ channel, thereby impairing the channel assembly via the activation of NF- κ B signaling cascade.⁴²

sEH inhibition increases epoxyeicosatrienoic acids, which has previously been shown to regulate gene expression via the inhibition of NF- κ B signaling.^{9,14} Of considerable

relevance are our findings that there is a significant upregulation of I_{to} from single isolated atrial myocytes and an inhibition of NF- κ B activation in cultured cells by treatment with sEHI. Taken together, our data support the notion that treatment with sEHI may reduce the electric remodeling in the atrial myocytes by the upregulation of outward transient K^+ current, possibly through the inhibition of the NF- κ B activation.

Translational Implications

The emergence of hiPSC technology has created a unique tool to study the effects of various drugs in both monogenetic diseases and in diseases with multiple pathogenesis, such as AF. Advantages of using hiPSC for drug screening include the ability to circumvent the problem of maintaining primary human cardiomyocytes in culture, the ability to obtain patient-specific cell lines and the ability to avoid adverse side effects of drugs.⁴³ In our study, we took advantage of hiPSC-CMs as a model system to study the effects of novel sEHI on the molecular mechanisms underlying the structural and electric remodeling in AF. Indeed, hiPSC-ACMs may be used as an in vitro drug-screening tool to study atrial arrhythmias. Finally, our study provides a proof-of-concept study for an upstream therapeutic target for the treatment of AF.

Sources of Funding

This study was supported by National Institutes of Health (NIH, R01 HL085727, R01 HL085844, and S10 RR033106 to Dr Chiamvimonvat), VA Merit Review Grant I01 BX000576 (to Dr Chiamvimonvat), American Heart Association Beginning Grant-in-Aid (14BGIA18870087 to Dr Zhang), and American Heart Association Postdoctoral Fellowship Award (16POST26970007 to Dr Sirish). Dr Sirish received a Postdoctoral Fellowship from California Institute for Regenerative Medicine Training Grant to UC Davis (TG2-01163) and an NIH/National Heart, Lung, and Blood Institute Institutional Training Grant in Basic and Translational Cardiovascular Science (T32 NIH HL086350). Dr Chiamvimonvat is the holder of the Roger Tatarian Endowed Professor in Cardiovascular Medicine. Other funding includes NIH K99 ES024806 (to Dr Lee); NIH K99DK100736 (to Dr Bettaieb); California Institute for Regenerative Medicine Basic Biology Grant (RB4-05764 to Dr Lieu); Harold Amos Medical Faculty Development award from the Robert Wood Johnson Foundation; and CTSC KL2 scholar supported by the National Center for Advancing Translational Sciences; NIH UL1 TR000002 (to Dr Lopez); NIH R01 DC003826, R01 DC007592, R01 DC010386, and R01 DC010917 (to Dr Yamoah); NIH R01DK090492 and R01DK095359 (to Dr Hajj); NIH R01 HL111600 (to Dr Ripplinger); and partial support from NIEHS R01 ES002710 and P42 ES04699 and the West Coast Metabolomics Center NIH U24 DK097154 (to Dr Hammock).

Disclosures

Drs Hammock and Chiamvimonvat have filed patents for the use of soluble epoxide hydrolase enzyme inhibitors in cardiomyopathy and arrhythmias. The other authors report no conflicts.

References

- Burstein B, Nattel S. Atrial fibrosis: mechanisms and clinical relevance in atrial fibrillation. *J Am Coll Cardiol*. 2008;51:802–809. doi: 10.1016/j.jacc.2007.09.064.
- Wilton SB, Fundytus A, Ghali WA, Veenhuizen GD, Quinn FR, Mitchell LB, Hill MD, Faris P, Exner DV. Meta-analysis of the effectiveness and

safety of catheter ablation of atrial fibrillation in patients with versus without left ventricular systolic dysfunction. *Am J Cardiol*. 2010;106:1284–1291. doi: 10.1016/j.amjcard.2010.06.053.

- Akiyama T, Pawitan Y, Greenberg H, Kuo CS, Reynolds-Haertle RA. Increased risk of death and cardiac arrest from encainide and flecainide in patients after non-Q-wave acute myocardial infarction in the Cardiac Arrhythmia Suppression Trial. CAST Investigators. *Am J Cardiol*. 1991;68:1551–1555.
- Everett TH IV, Olgin JE. Atrial fibrosis and the mechanisms of atrial fibrillation. *Heart Rhythm*. 2007;4(suppl 3):S24–S27. doi: 10.1016/j.hrthm.2006.12.040.
- Guo Y, Lip GY, Apostolakis S. Inflammation in atrial fibrillation. *J Am Coll Cardiol*. 2012;60:2263–2270. doi: 10.1016/j.jacc.2012.04.063.
- Sun M, Chen M, Dawood F, Zurawska U, Li JY, Parker T, Kassiri Z, Kirshenbaum LA, Arnold M, Khokha R, Liu PP. Tumor necrosis factor- α mediates cardiac remodeling and ventricular dysfunction after pressure overload state. *Circulation*. 2007;115:1398–1407. doi: 10.1161/CIRCULATIONAHA.106.643585.
- Harada M, Van Wagoner DR, Nattel S. Role of inflammation in atrial fibrillation pathophysiology and management. *Circ J*. 2015;79:495–502. doi: 10.1253/circj.CJ-15-0138.
- Corradi D, Callegari S, Maestri R, Benussi S, Alfieri O. Structural remodeling in atrial fibrillation. *Nat Clin Pract Cardiovasc Med*. 2008;5:782–796. doi: 10.1038/npcardio.1370.
- Spector AA, Fang X, Snyder GD, Weintraub NL. Epoxyeicosatrienoic acids (EETs): metabolism and biochemical function. *Prog Lipid Res*. 2004;43:55–90.
- Morisseau C, Hammock BD. Epoxide hydrolases: mechanisms, inhibitor designs, and biological roles. *Annu Rev Pharmacol Toxicol*. 2005;45:311–333. doi: 10.1146/annurev.pharmtox.45.120403.095920.
- Li N, Liu JY, Qiu H, Harris TR, Sirish P, Hammock BD, Chiamvimonvat N. Use of metabolomic profiling in the study of arachidonic acid metabolism in cardiovascular disease. *Congest Heart Fail*. 2011;17:42–46. doi: 10.1111/j.1751-7133.2010.00209.x.
- Li N, Liu JY, Timofeyev V, Qiu H, Hwang SH, Tuteja D, Lu L, Yang J, Mochida H, Low R, Hammock BD, Chiamvimonvat N. Beneficial effects of soluble epoxide hydrolase inhibitors in myocardial infarction model: Insight gained using metabolomic approaches. *J Mol Cell Cardiol*. 2009;47:835–845. doi: 10.1016/j.yjmcc.2009.08.017.
- Sirish P, Li N, Liu JY, Lee KS, Hwang SH, Qiu H, Zhao C, Ma SM, López JE, Hammock BD, Chiamvimonvat N. Unique mechanistic insights into the beneficial effects of soluble epoxide hydrolase inhibitors in the prevention of cardiac fibrosis. *Proc Natl Acad Sci U S A*. 2013;110:5618–5623. doi: 10.1073/pnas.1221972110.
- Xu D, Li N, He Y, Timofeyev V, Lu L, Tsai HJ, Kim IH, Tuteja D, Mateo RK, Singapurri A, Davis BB, Low R, Hammock BD, Chiamvimonvat N. Prevention and reversal of cardiac hypertrophy by soluble epoxide hydrolase inhibitors. *Proc Natl Acad Sci U S A*. 2006;103:18733–18738. doi: 10.1073/pnas.0609158103.
- Lian X, Zhang J, Azarin SM, Zhu K, Hazeltine LB, Bao X, Hsiao C, Kamp TJ, Palecek SP. Directed cardiomyocyte differentiation from human pluripotent stem cells by modulating Wnt/ β -catenin signaling under fully defined conditions. *Nat Protoc*. 2013;8:162–175. doi: 10.1038/nprot.2012.150.
- Sirish P, López JE, Li N, Wong A, Timofeyev V, Young JN, Majidi M, Li RA, Chen HS, Chiamvimonvat N. MicroRNA profiling predicts a variance in the proliferative potential of cardiac progenitor cells derived from neonatal and adult murine hearts. *J Mol Cell Cardiol*. 2012;52:264–272. doi: 10.1016/j.yjmcc.2011.10.012.
- De Jesus NM, Wang L, Herren AW, Wang J, Shenasa F, Bers DM, Lindsey ML, Ripplinger CM. Atherosclerosis exacerbates arrhythmia following myocardial infarction: Role of myocardial inflammation. *Heart Rhythm*. 2015;12:169–178. doi: 10.1016/j.hrthm.2014.10.007.
- Li L, Li N, Pang W, Zhang X, Hammock BD, Ai D, Zhu Y. Opposite effects of gene deficiency and pharmacological inhibition of soluble epoxide hydrolase on cardiac fibrosis. *PLoS One*. 2014;9:e94092. doi: 10.1371/journal.pone.0094092.
- Aharinejad S, Krenn K, Paulus P, Schäfer R, Zuckermann A, Grimm M, Abraham D. Differential role of TGF- β 1/bFGF and ET-1 in graft fibrosis in heart failure patients. *Am J Transplant*. 2005;5:2185–2192. doi: 10.1111/j.1600-6143.2005.01006.x.
- Hanna N, Cardin S, Leung TK, Nattel S. Differences in atrial versus ventricular remodeling in dogs with ventricular tachypacing-induced congestive heart failure. *Cardiovasc Res*. 2004;63:236–244. doi: 10.1016/j.cardiores.2004.03.026.

21. Burstein B, Libby E, Calderone A, Nattel S. Differential behaviors of atrial versus ventricular fibroblasts: a potential role for platelet-derived growth factor in atrial-ventricular remodeling differences. *Circulation*. 2008;117:1630–1641. doi: 10.1161/CIRCULATIONAHA.107.748053.
22. Levine B, Kalman J, Mayer L, Fillit HM, Packer M. Elevated circulating levels of tumor necrosis factor in severe chronic heart failure. *N Engl J Med*. 1990;323:236–241. doi: 10.1056/NEJM199007263230405.
23. Rahmutula D, Marcus GM, Wilson EE, Ding CH, Xiao Y, Paquet AC, Barbeau R, Barczak AJ, Erle DJ, Olgin JE. Molecular basis of selective atrial fibrosis due to overexpression of transforming growth factor- β 1. *Cardiovasc Res*. 2013;99:769–779. doi: 10.1093/cvr/cvt074.
24. Kupfahl C, Pink D, Friedrich K, Zurbrügg HR, Neuss M, Warnecke C, Fielitz J, Graf K, Fleck E, Regitz-Zagrosek V. Angiotensin II directly increases transforming growth factor beta1 and osteopontin and indirectly affects collagen mRNA expression in the human heart. *Cardiovasc Res*. 2000;46:463–475.
25. Dobaczewski M, Chen W, Frangogiannis NG. Transforming growth factor (TGF)- β signaling in cardiac remodeling. *J Mol Cell Cardiol*. 2011;51:600–606. doi: 10.1016/j.yjmcc.2010.10.033.
26. Björnstad JL, Skrbic B, Marstein HS, Hasic A, Sjaastad I, Louch WE, Florholmen G, Christensen G, Tønnessen T. Inhibition of SMAD2 phosphorylation preserves cardiac function during pressure overload. *Cardiovasc Res*. 2012;93:100–110. doi: 10.1093/cvr/cvr294.
27. Jalife J, Kaur K. Atrial remodeling, fibrosis, and atrial fibrillation. *Trends Cardiovasc Med*. 2015;25:475–484. doi: 10.1016/j.tcm.2014.12.015.
28. Sovari AA, Dudley SC Jr. Reactive oxygen species-targeted therapeutic interventions for atrial fibrillation. *Front Physiol*. 2012;3:311. doi: 10.3389/fphys.2012.00311.
29. Kamakura T, Makiyama T, Sasaki K, Yoshida Y, Wuriyanghai Y, Chen J, Hattori T, Ohno S, Kita T, Horie M, Yamanaka S, Kimura T. Ultrastructural maturation of human-induced pluripotent stem cell-derived cardiomyocytes in a long-term culture. *Circ J*. 2013;77:1307–1314.
30. Park CS, Cha H, Kwon EJ, Sreenivasaiah PK, Kim do H. The chemical chaperone 4-phenylbutyric acid attenuates pressure-overload cardiac hypertrophy by alleviating endoplasmic reticulum stress. *Biochem Biophys Res Commun*. 2012;421:578–584. doi: 10.1016/j.bbrc.2012.04.048.
31. Luo T, Kim JK, Chen B, Abdel-Latif A, Kitakaze M, Yan L. Attenuation of ER stress prevents post-infarction-induced cardiac rupture and remodeling by modulating both cardiac apoptosis and fibrosis. *Chem Biol Interact*. 2015;225:90–98. doi: 10.1016/j.cbi.2014.10.032.
32. Harris TR, Bettaieb A, Kodani S, Dong H, Myers R, Chiamvimonvat N, Haj FG, Hammock BD. Inhibition of soluble epoxide hydrolase attenuates hepatic fibrosis and endoplasmic reticulum stress induced by carbon tetrachloride in mice. *Toxicol Appl Pharmacol*. 2015;286:102–111. doi: 10.1016/j.taap.2015.03.022.
33. Bettaieb A, Chahed S, Tabet G, Yang J, Morisseau C, Griffey S, Hammock BD, Haj FG. Effects of soluble epoxide hydrolase deficiency on acute pancreatitis in mice. *PLoS One*. 2014;9:e113019. doi: 10.1371/journal.pone.0113019.
34. Groenendyk J, Agellon LB, Michalak M. Coping with endoplasmic reticulum stress in the cardiovascular system. *Annu Rev Physiol*. 2013;75:49–67. doi: 10.1146/annurev-physiol-030212-183707.
35. Olsen NT, Dimaano VL, Fritz-Hansen T, Sogaard P, Chakir K, Eskesen K, Steenbergen C, Kass DA, Abraham TP. Hypertrophy signaling pathways in experimental chronic aortic regurgitation. *J Cardiovasc Transl Res*. 2013;6:852–860. doi: 10.1007/s12265-013-9503-y.
36. Ripplinger CM, Lou Q, Li W, Hadley J, Efimov IR. Panoramic imaging reveals basic mechanisms of induction and termination of ventricular tachycardia in rabbit heart with chronic infarction: implications for low-voltage cardioversion. *Heart Rhythm*. 2009;6:87–97. doi: 10.1016/j.hrthm.2008.09.019.
37. Kistler PM, Sanders P, Dodic M, Spence SJ, Samuel CS, Zhao C, Charles JA, Edwards GA, Kalman JM. Atrial electrical and structural abnormalities in an ovine model of chronic blood pressure elevation after prenatal corticosteroid exposure: implications for development of atrial fibrillation. *Eur Heart J*. 2006;27:3045–3056. doi: 10.1093/eurheartj/ehl360.
38. Castillero E, Akashi H, Pendrak K, Yerebakan H, Najjar M, Wang C, Naka Y, Mancini D, Sweeney HL, D Armiento J, Ali ZA, Schulze PC, George I. Attenuation of the unfolded protein response and endoplasmic reticulum stress after mechanical unloading in dilated cardiomyopathy. *Am J Physiol Heart Circ Physiol*. 2015;309:H459–H470. doi: 10.1152/ajpheart.00056.2015.
39. Zhang W, Elimban V, Nijjar MS, Gupta SK, Dhalla NS. Role of mitogen-activated protein kinase in cardiac hypertrophy and heart failure. *Exp Clin Cardiol*. 2003;8:173–183.
40. Wakili R, Voigt N, Kääh S, Dobrev D, Nattel S. Recent advances in the molecular pathophysiology of atrial fibrillation. *J Clin Invest*. 2011;121:2955–2968. doi: 10.1172/JCI46315.
41. Brandt MC, Priebe L, Böhle T, Südkamp M, Beuckelmann DJ. The ultra-rapid and the transient outward K(+) current in human atrial fibrillation. Their possible role in postoperative atrial fibrillation. *J Mol Cell Cardiol*. 2000;32:1885–1896. doi: 10.1006/jmcc.2000.1221.
42. Panama BK, Latour-Villamil D, Farman GP, Zhao D, Bolz SS, Kirshenbaum LA, Backx PH. Nuclear factor kappaB downregulates the transient outward potassium current I(to,f) through control of KChIP2 expression. *Circ Res*. 2011;108:537–543. doi: 10.1161/CIRCRESAHA.110.229112.
43. Sinnecker D, Goedel A, Laugwitz KL, Moretti A. Induced pluripotent stem cell-derived cardiomyocytes: a versatile tool for arrhythmia research. *Circ Res*. 2013;112:961–968. doi: 10.1161/CIRCRESAHA.112.268623.

Molecular Mechanisms and New Treatment Paradigm for Atrial Fibrillation

Padmini Sirish, Ning Li, Valeriy Timofeyev, Xiao-Dong Zhang, Lianguo Wang, Jun Yang, Kin Sing Stephen Lee, Ahmed Bettaieb, Sin Mei Ma, Jeong Han Lee, Demetria Su, Victor C. Lau, Richard E. Myers, Deborah K. Lieu, Javier E. López, J. Nilas Young, Ebenezer N. Yamoah, Fawaz Haj, Crystal M. Ripplinger, Bruce D. Hammock and Nipavan Chiamvimonvat

Circ Arrhythm Electrophysiol. 2016;9:

doi: 10.1161/CIRCEP.115.003721

Circulation: Arrhythmia and Electrophysiology is published by the American Heart Association, 7272 Greenville Avenue, Dallas, TX 75231

Copyright © 2016 American Heart Association, Inc. All rights reserved.

Print ISSN: 1941-3149. Online ISSN: 1941-3084

The online version of this article, along with updated information and services, is located on the World Wide Web at:

<http://circep.ahajournals.org/content/9/5/e003721>

Data Supplement (unedited) at:

<http://circep.ahajournals.org/content/suppl/2016/05/10/CIRCEP.115.003721.DC1.html>

Permissions: Requests for permissions to reproduce figures, tables, or portions of articles originally published in *Circulation: Arrhythmia and Electrophysiology* can be obtained via RightsLink, a service of the Copyright Clearance Center, not the Editorial Office. Once the online version of the published article for which permission is being requested is located, click Request Permissions in the middle column of the Web page under Services. Further information about this process is available in the [Permissions and Rights Question and Answer](#) document.

Reprints: Information about reprints can be found online at:
<http://www.lww.com/reprints>

Subscriptions: Information about subscribing to *Circulation: Arrhythmia and Electrophysiology* is online at:
<http://circep.ahajournals.org/subscriptions/>

DATA SUPPLEMENT

Supplemental Materials and Methods

Soluble epoxide hydrolase inhibitor (sEHI):

Selective and potent inhibitors (low nanomolar K_i 's) for rodent and human sEH were developed based on the catalytic mechanism and the X-ray structure of the murine sEH (PDB access #: 1CQZ & 1CR6).¹⁻³ The potency, pharmacokinetics, and physicochemical properties of 11 different sEHIs were conducted. 1-Trifluoromethoxyphenyl-3-(1-propionylpiperidine-4-yl)urea (TPPU, containing a piperidine ring, Figure 1A) was found to have high inhibitory potency, drug-like physicochemical properties, pharmacokinetics with high area under the curve values, a relatively longer half-life and lower plasma protein binding properties than many previous compounds.⁴ For these pharmacokinetic favorable characteristics, TPPU was chosen for this study. TPPU was found to be a low nanomolar inhibitor of the sEH enzyme and was previously tested against commercial drug targets and the NIH screen of drug targets, there were no hits at 10 micromolar (over 1,000 fold higher concentration than the effective concentration for the sEH enzyme). In addition, the X-ray crystal structure of the soluble epoxide enzyme and the inhibitors has been solved.⁵⁻¹² There is no evidence to date of off-target binding sites.

Thoracic Aortic Constriction (TAC) model in mice:

TACs were performed in 8- to 12-week-old male C57BL/6J mice (Charles River, Wilmington, MA) as previously described.¹³ Mice from the same litters were used for sham, sham-TPPU treatment, TAC and TAC-TPPU treatment. Briefly, animals were anesthetized with i.p. ketamine 50 mg/kg and xylazine 2.5 mg/kg. Intubation was performed perorally and mechanical ventilation was initiated. Aortic constriction was created *via* a left thoracotomy by placing a ligature securely around the ascending aorta and a 26-gauge needle and then removing the needle. The chest was closed with 3-0 dextron rib sutures, 5-0 dextron II muscle sutures and buried skin sutures. Negative pleural pressure was re-established *via* a

temporary chest tube until spontaneous breathing occurs. Sham-operated animals underwent the same procedure without tying the suture. Echocardiograms were performed 1 week after surgery after which mice were randomized to receive TPPU (15 mg/L)¹⁴ in the drinking water or water alone for a period of 3 weeks. Four groups of animals including sham, sham treated with TPPU, TAC, and TAC treated with TPPU were followed for a period of three weeks at which time repeat echocardiograms were performed.

Analysis of cardiac function by echocardiography:

Echocardiograms to assess systolic function were performed by using M-mode and two-dimensional measurements as described previously.¹⁵ The measurements represented the average of six selected cardiac cycles from at least two separate scans performed in a blinded fashion with papillary muscles used as a point of reference for consistency in the level of scan. Fractional shortening (FS), a surrogate of systolic function, was calculated from left ventricle dimensions as follows: %FS = ((EDD-ESD)/EDD) x100, where EDD and ESD represent end-diastolic and end-systolic dimensions, respectively.

Histological analyses:

Hearts were excised and retrogradely perfused with phosphate-buffered solution to wash out blood and fixed in 10% formalin overnight. Hearts were then embedded in paraffin, serial left atrial (LA) and right atrial (RA) cardiac sections of 5 µm in thickness were taken along the longitudinal axis and stained with Picrosirius Red to assess for collagen content.

Immunofluorescence confocal laser scanning microscopy:

Additional cardiac sections were stained with wheat germ agglutinin (WGA). The cardiac sections were deparaffinized with Xylene before rehydrating with serial dilution of ethanol. The sections were blocked with donkey serum and stained with WGA-conjugated to Alexafluor-488 (10 µg ml⁻¹,

Molecular Probes). Cardiac sections from corresponding area from the four groups were scanned. Identical settings were used for all the specimens. Immunofluorescence-labeled images were obtained using a Zeiss LSM700 confocal laser-scanning microscope.

Flow cytometric analysis of cardiac cells:

Single cell suspension was obtained from 8- to 12-week-old male C57BL/6 mice as previously described.¹⁶ The procedure was performed according to the approved UC Davis Animal Care and Use protocol. Briefly, mice were injected with 0.1 ml heparin (1,000 units ml⁻¹) 10 min prior to heart excision, then anesthetized with pentobarbital intraperitoneally (80 mg kg⁻¹). Hearts were removed and placed in Tyrode's solution (mmol l⁻¹: NaCl 140, KCl 5.4, MgCl₂ 1.2, *N*-2-hydroxyethylpiperazine-*N'*-2-ethanesulphonic acid (HEPES) 5 and glucose 5, pH 7.4). All chemicals were obtained from Sigma Chemicals (St. Louis, MO) unless stated otherwise. The aorta was cannulated under a dissecting microscope and mounted on the Langendorff apparatus. The coronary arteries were retrogradely perfused with Tyrode's solution gassed with O₂ at 37 °C for 3 min at a flow rate of ~3 ml min⁻¹. The solution was switched to Tyrode's solution containing collagenase type 2 (1 mg ml⁻¹, 330 units mg⁻¹, Worthington Biochemical Corporation). After ~12 min of enzyme perfusion, hearts were removed from the perfusion apparatus and gently teased in high-K⁺ solution (mmol l⁻¹: potassium glutamate 120, KCl 20, MgCl₂ 1, EGTA 0.3, glucose 10 and HEPES 10, pH 7.4 with KOH). Cells were filtered through 200 µm cell strainer, re-suspended in Ca²⁺ and Mg²⁺ free phosphate buffered saline (PBS), fixed with 0.4% paraformaldehyde (PFA), treated with methanol before treating with phytoerythrin-conjugated anti-Thy1.2 (BD Bioscience, San Diego, CA), lineage antibody cocktail (CD3e, CD11b, Cd45R, Ly-6C, Ly-6G and TER-119, 1:100 dilution, BD Bioscience), anti-CD45 (BD Bioscience, San Diego, CA), anti-troponin T antibody (Thermo Scientific), anti-CD31 (BD Bioscience), Alexa fluor 488 or 647-conjugated anti-pERK1/2 (Cell Signaling), Alexa fluor 647-conjugated anti-pSMAD2/3 (BD Bioscience), and proliferation-specific Ki67 antibody (15 µg ml⁻¹, BD Bioscience) in PBS with 5% donkey serum and 20 µg ml⁻¹ DNase-free RNase (Sigma) overnight at 4°C. Cells were also stained with 40 µg ml⁻¹ 7-amino-

actinomycin D (7AAD, BD Bioscience, San Jose, CA) to measure the DNA content. Equal number of atrial myocytes (left and right together) were isolated from sham, sham-TPPU treated, TAC and TAC-TPPU treated hearts and 10,000 to 20,000 cells were analyzed in each run. Data were collected using a standard FACScan cytometer (BD Biosciences, San Jose, CA) upgraded to a dual laser system with the addition of a blue laser (15 mW at 488 nm) and a red laser (25 mW at 637 nm Cyttek Development, Inc, Fremont, CA). Data were acquired using CellQuest software (BD Bioscience) and analyzed using FlowJo software (ver9.4 Treestar Inc., San Carlos). Cells stained with isotype-matched IgG antibodies were used as controls to determine the positive cell population.

In vitro human cardiac fibroblast culture:

Human right atrial appendage specimens from informed consented patients undergoing cardiac bypass surgery were obtained from UC Davis Medical Center in accordance with the approved UC Davis Institutional Review Board (IRB) protocol. The tissue was stored in cardioplegic solution at 4°C and processed within 2 hours. The cardiac tissue was washed and minced in filter-sterilized (0.2 µm) Ca²⁺-and bicarbonate-free Hanks' buffer with HEPES (CBFHH) solution (mmol l⁻¹: NaCl 137, KCl 5.36, MgSO₄ 0.81, HEPES 20.06, K₂PO₄ 0.44, and Na₂HPO₄ 0.34, pH 7.4) at room temperature. The tissue pieces were digested with CBFHH solution containing 2% bovine serum albumin, 0.1% collagenase type 2 and 0.2% trypsin with continuous stirring at 37°C for 3 min. The supernatant was discarded and the enzyme solution replaced for 10 min and repeated for 3 min. The partially dissociated pieces were washed with medium before plating on cell culture dishes and maintained in DMEM/F12 medium (10% fetal bovine serum and 1% penicillin/streptomycin) until the appearance of fibroblasts from the explants. The cells were trypsinized and plated on 12 well plates until confluency and treated with angiotensin II (Sigma and 1 µM for 24 hours) and TPPU (1 µM) before flow cytometric analysis with phytoerythrin-conjugated anti-Thy1.1 (BD Bioscience, San Diego, CA), FITC conjugated lineage antibody cocktail (CD3, CD14, CD19, CD20 and CD56 BD Bioscience), APC-Cy7-conjugated anti-CD45 (BD Bioscience, San Diego, CA) and proliferation-specific Ki67 antibody (15 µg ml⁻¹, BD Bioscience).

Human-induced pluripotent stem cell-derived cardiomyocytes (hiPSC-CM) and hiPSC-derived cardiac fibroblasts:

HiPSC were plated and differentiated for 20 days using a directed differentiation protocol.¹⁷ HiPSC-CMs enriched with puromycin and treated with Tumor Necrosis Factor- α (TNF- α) or angiotensin II (ANG II) and TPPU were fixed and stained with anti- α -actinin, anti-NF- κ B, anti-myosin light chain-2a (MLC2a), anti-myosin light chain-2v (MLC2v) and fibroblast-specific antibodies. HiPSC-derived cardiac fibroblasts were defined as Thy1.1⁺/Lin⁻/CD45⁻ cells (hiPSC-Thy^{pos} cells). Differentiated hiPSCs at day 20 were treated with angiotensin II (Sigma and 1 μ M for 24 hours) or TNF- α (20 ng/ml for 20 minutes) and TPPU (1 μ M) before flow cytometric analyses as described above.

Western Blot Analysis:

Immunoblots were performed as previously described¹⁶ using anti-I κ B (1:1000, Cell Signaling), anti-phospho-I κ B (1:1000, Cell Signaling), anti-NF- κ B (1:1000, Cell Signaling) and anti-GAPDH (1:10000, Fitzgerald) antibodies.

Measurement of Plasma Cytokine Levels:

Plasma samples were collected 3 weeks after sham or TAC operation and stored at -80 °C until assayed. Plasma cytokine levels were analyzed using a Cytometric Bead Array kit (CBA mouse inflammation kit, BD Biosciences). Briefly, thawed plasma samples were mixed for 2 hours at room temperature with fluorescence-labeled capture beads with the PE detection reagents to measure the concentrations of Interleukin-6 (IL-6), Interleukin-10 (IL-10), Monocyte Chemoattractant Protein-1 (MCP-1), Interferon- γ (INF- γ), Tumor necrosis factor- α (TNF- α), and Interleukin-12p70 (IL-12 p70). Samples were then washed with washing buffer and analyzed on a FACScan flow cytometer (BD Immunocytometry Systems). Data were analyzed using BD Cytometric Bead Array Analysis software (BD Immunocytometry Systems).

Metabolomic Profiling of Oxylipins:

Plasma samples stored at -80 °C were thawed at room temperature. Aliquots of plasma (200 µL) were spiked with a set of odd chain length analogs and deuterated isomers of several target analytes including hydroxyeicosatetraenoic acids (HETEs), prostaglandins, thromboxanes, epoxides (EpOMEs and EETs), and diols (DHOMEs and DHETs) contained in 10 µL of methanol, and then were extracted by solid phase extraction using Oasis HLB cartridges (Waters, Milford, MA). The HLB columns (1 cc, 60 mg) were washed with 2 mL methanol and pre-conditioned with 2 mL water/methanol/acetic acid (95/5/0.1, v/v). Samples were then mixed with 200 µL of the pre-conditioning solution and loaded onto the column. The loaded column was then washed with 2 mL of the pre-conditioning solution and then dried for 5 min *in vacuo*. Target analytes were then eluted with 2 mL of ethyl acetate. The collected eluents were evaporated to dryness using a centrifugal vacuum concentrator and re-dissolved in 40 µL of methanol. The spiked samples were vortexed for 1 min, centrifuged at 14,000 r.p.m. for 5 min, and then transferred to analytical vials containing 150 µL inserts for analysis.

The oxylipin profiling was performed using a previously published method.¹³ The separation of plasma oxylipins was conducted in a Shimadzu LC-10AD_{VP} instrument (Shimadzu Corp., Kyoto, Japan) equipped with a 2.1 mm X 150 mm Pursuit XR_S-C18 5 µm column (Varian Inc, Palo Alto, CA) held at 40 °C. A gradient of water containing 0.1% acetic acid (v/v, solvent A) and acetonitrile/methanol/acetic acid (800/150/1, v/v; solvent B) was used to elute the column with the flow rate of 0.4 mL min⁻¹ (SI Table 1). The injection volume was 10 µL and the samples were kept at 10 °C in the auto sampler. Analytes were detected on a 4000 QTRAP (Applied Biosystems, Foster City, CA) hybrid, triple-quadrupole, and linear ion trap mass spectrometer equipped with a Turbo V ion source and operated in negative MRM mode. The source was operated in negative electrospray mode and the QTRAP was set as follows: CUR=20 psi, GS1=50 psi, GS2=30 psi, IS=-4500 V, CAD= HIGH, TEM=400°C, ihe=ON, DP=-60 V. The collision energies used for CAD ranged from -18 to -38 eV.

Evaluation of Endoplasmic Reticulum (ER) Stress markers:

Atrial tissues were homogenized in RIPA buffer supplemented with protease inhibitors and phosphatase inhibitors (10 mM Tris-HCl, pH 7.4, 150 mM NaCl, 0.1% sodium dodecyl sulfate, 1% TritonX-100, 1% sodium deoxycholate, 5 mM EDTA, 1 mM NaF, 1 mM sodium orthovanadate and protease inhibitors). Lysates were clarified by centrifugation at 13,000 rpm for 10 min and protein concentrations were determined using bicinchoninic acid protein assay kit (Pierce Chemical). Proteins were resolved by SDS-PAGE and transferred to PVDF membranes. Immunoblotting of lysates was performed with antibodies for pp38 (Thr180/Tyr182), p38, pJNK (Thr183/Tyr185), JNK, (Cell Signaling Technology; Danvers, MA), pPERK (Thr980), PERK, peIF2 α (Ser51), eIF2 α , sXBP1, IRE1 α and Tubulin (all from Santa Cruz Biotechnology; Santa Cruz, CA). Antibody for pIRE1 α (Ser724) was obtained from Abcam, Cambridge, MA. After incubation with the appropriate secondary antibodies, proteins were visualized using enhanced chemiluminescence (ECL, Amersham Biosciences). Pixel intensities of immunoreactive bands were quantified using ImageQuant 5.0 software (Molecular Dynamics). Data for phosphorylated proteins are presented as phosphorylation level normalized to total protein expression and for non-phosphorylated proteins as total protein expression normalized to β -tubulin, which remains unchanged in the four groups. **Fig S5j**).

Ex vivo Optical Mapping of transmembrane potential (V_m):

Langendorff perfusion and optical mapping of V_m were carried out as described previously.¹⁸ Briefly, mice were anesthetized with pentobarbital sodium (150 mg/kg, I.P.) containing 120 IU of heparin. Following a mid-sternal incision, hearts were rapidly removed and perfused in a $37\pm 0.5^\circ\text{C}$ Tyrode's solution of the following composition (in mmol/L): NaCl 128.2, CaCl₂ 1.3, KCl 4.7, MgCl₂ 1.05, NaH₂PO₄ 1.19, NaHCO₃ 20 and glucose 11.1 (pH 7.4 ± 0.05). Flow rate (1.5-3.5 mL/min) was adjusted to maintain a perfusion pressure of 60-80 mmHg. The hearts were placed in a perfusion dish with the posterior surface of the heart facing the optical mapping camera. In addition to coronary perfusion, the hearts were submerged in the solution and superfused in the dish to keep the temperature at $37\pm 0.5^\circ\text{C}$.

The atrial appendages were pinned in the dish with fine insect pins to elevate the posterior epicardium of the atrial appendages into the focal plane for imaging. A bipolar pacing electrode was positioned on the epicardium of left or right atrial appendage for pacing using a 2 ms pulse at twice the diastolic threshold. Blebbistatin (10-20 μ M, Tocris Bioscience, Ellisville, MO) was added to the perfusate to reduce motion artifacts during optical recordings (Fedorov VV et al., Heart Rhythm, 2007). The heart was stained with the voltage-sensitive dye (RH237, 5 μ L of 1 mg/mL in DMSO, Molecular Probes) via the coronary perfusion. Excitation light was produced with two continuous-wave LED sources centered at 531 nm and bandpass filtered from 511-551 nm (LEX-2, SciMedia, Costa Mesa, CA). The emitted fluorescence was collected through an objective (Leica, 1x) and the fluorescence signal longpass filtered at 700 nm. Optical action potentials were recorded using a 16-bit complementary metal oxide camera (CMOS, MiCam Ultima-L, SciMedia, Costa Mesa, CA). Images were acquired at 1 kHz and 100x100 pixels with a 10x10 mm field of view.

Baseline electrophysiological parameters were determined during atrial epicardial pacing at a pacing cycle length (PCL) of 100 ms. Effective refractory period (ERP) was determined using a standard S1-S2 pacing protocol (18 S1s at 100ms followed by a premature S2 stimulus decreasing by 5-10 ms until the ERP was reached). ERP was measured from both the left and right atrium. Data analysis was performed using a commercially available analysis program (*Optiq*, Cairn, UK). The V_m signals were post-processed using a spatial Gaussian filter (3x3 pixels). Action potential (AP) characteristics were analyzed from data collected during pacing at a PCL of 100 ms from the left appendage. AP activation time was determined as the time at 50% between peak and baseline amplitude. Action potential duration at 80% repolarization (APD_{80}) was calculated as repolarization time – activation time from data collected during pacing at 100 ms (S1) or 60 ms (S2) on the left or right atrial appendage. Pseudo-color AP activation and APD_{80} maps were generated from measurements of activation time and APD_{80} at individual pixels. The sizes and shapes of the maps were selected based on the signal-to-noise ratio levels of the mapping area that allow for proper analysis.

Electrophysiological studies of single isolated atrial myocytes:

Atrial myocytes were isolated from hearts using previously described protocol.¹⁵ Briefly, hearts were removed, and retrogradely perfused with collagenase B (Boehringer Mannheim) and 3 mg protease (type XIV, 4.5 units/mg, Sigma). Experiments were performed using the conventional whole-cell patch-clamp technique at room temperature.¹⁵ For K⁺ current recording, the external solution contained (mM) NMG 130, KCl 5, CaCl₂ 1, MgCl₂ 1, Nimodipine 1 μM, glucose 10, HEPES 10, pH 7.4 with HCl. The pipette solution contained (mM) KCl 140, Mg-ATP 4, MgCl₂ 1, EGTA 10, HEPES 10, pH 7.4 with KOH. All experiments were performed using 3 M KCl agar bridges. Cell capacitance was calculated as the ratio of total charge (the integrated area under the current transient) to the magnitude of the pulse (20 mV). Currents were normalized to cell capacity to obtain the current density. The series resistance was compensated electronically. In all experiments, a series resistance compensation of 90% was obtained. Currents were recorded using Axopatch 200B amplifier (Axon 7 Instrument), filtered at 10 kHz using a 4-pole Bessel filter and digitized at sampling frequency of 50 kHz. Data analysis was carried out using custom-written software and commercially available PC-based spreadsheet and graphics software (MicroCal Origin version 6.0).

Statistical Analysis:

Data are presented as mean ± S.E.M. Statistical comparisons were analyzed by one-way ANOVA followed by Bonferroni tests and Tukey's-Kramer honest significant difference analyses for post hoc comparison. Statistical significance was considered to be achieved when $p < 0.05$ and $p < 0.01$ (for ER Stress assay).

Supplemental References

1. Argiriadi MA, Morisseau C, Goodrow MH, Dowdy DL, Hammock BD, Christianson DW. Binding of alkylurea inhibitors to epoxide hydrolase implicates active site tyrosines in substrate activation. *J Biol Chem.* 2000;275:15265-15270.
2. Argiriadi MA, Morisseau C, Hammock BD, Christianson DW. Detoxification of environmental mutagens and carcinogens: structure, mechanism, and evolution of liver epoxide hydrolase. *Proc Natl Acad Sci U S A.* 1999;96:10637-10642.
3. Morisseau C, Goodrow MH, Dowdy D, Zheng J, Greene JF, Sanborn JR, Hammock BD. Potent urea and carbamate inhibitors of soluble epoxide hydrolases. *Proc Natl Acad Sci U S A.* 1999;96:8849-8854.
4. Ulu A, Appt S, Morisseau C, Hwang SH, Jones PD, Rose TE, Dong H, Lango J, Yang J, Tsai HJ, Miyabe C, Fortenbach C, Adams MR, Hammock BD. Pharmacokinetics and in vivo potency of soluble epoxide hydrolase inhibitors in cynomolgus monkeys. *Br J Pharmacol.* 2012;165:1401-1412.
5. Gomez GA, Morisseau C, Hammock BD, Christianson DW. Structure of human epoxide hydrolase reveals mechanistic inferences on bifunctional catalysis in epoxide and phosphate ester hydrolysis. *Biochemistry.* 2004;43:4716-4723.
6. Gomez GA, Morisseau C, Hammock BD, Christianson DW. Human soluble epoxide hydrolase: structural basis of inhibition by 4-(3-cyclohexylureido)-carboxylic acids. *Protein Science.* 2006;15:58-64.
7. Garriga M, Caballero J. Insights into the structure of urea-like compounds as inhibitors of the juvenile hormone epoxide hydrolase (JHEH) of the tobacco hornworm *Manduca sexta*: analysis of the binding modes and structure-activity relationships of the inhibitors by docking and CoMFA calculations. *Chemosphere.* 2011;82:1604-1613.

8. Xing L, McDonald JJ, Kolodziej SA, Kurumbail RG, Williams JM, Warren CJ, O'Neal JM, Skepner JE, Roberds SL. Discovery of potent inhibitors of soluble epoxide hydrolase by combinatorial library design and structure-based virtual screening. *J Med Chem.* 2011;54:1211-1222.
9. Moser D, Achenbach J, Klingler FM, Estel la B, Hahn S, Proschak E. Evaluation of structure-derived pharmacophore of soluble epoxide hydrolase inhibitors by virtual screening. *Bioorganic Medicinal Chem Lett.* 2012;22:6762-6765.
10. Amano Y, Yamaguchi T, Tanabe E. Structural insights into binding of inhibitors to soluble epoxide hydrolase gained by fragment screening and X-ray crystallography. *Bioorganic Medicinal Chem.* 2014;22:2427-2434.
11. Takai K, Chiyo N, Nakajima T, Nariai T, Ishikawa C, Nakatani S, Ikeno A, Yamamoto S, Sone T. Three-dimensional rational approach to the discovery of potent substituted cyclopropyl urea soluble epoxide hydrolase inhibitors. *Bioorganic Medicinal Chem Lett.* 2015;25:1705-1708.
12. Amano Y, Tanabe E, Yamaguchi T. Identification of N-ethylmethylanine as a novel scaffold for inhibitors of soluble epoxide hydrolase by crystallographic fragment screening. *Bioorganic Medicinal Chem.* 2015;23:2310-2317.
13. Sirish P, Li N, Liu JY, Lee KS, Hwang SH, Qiu H, Zhao C, Ma SM, Lopez JE, Hammock BD, Chiamvimonvat N. Unique mechanistic insights into the beneficial effects of soluble epoxide hydrolase inhibitors in the prevention of cardiac fibrosis. *Proc Natl Acad Sci U S A.* 2013;110:5618-5623.
14. Hwang SH, Tsai HJ, Liu JY, Morisseau C, Hammock BD. Orally bioavailable potent soluble epoxide hydrolase inhibitors. *J Med Chem.* 2007;50:3825-3840.
15. Li N, Liu JY, Timofeyev V, Qiu H, Hwang SH, Tuteja D, Lu L, Yang J, Mochida H, Low R, Hammock BD, Chiamvimonvat N. Beneficial effects of soluble epoxide hydrolase inhibitors in myocardial infarction model: Insight gained using metabolomic approaches. *J Mol Cell Cardiol.* 2009;47:835-845.

16. Sirish P, Lopez JE, Li N, Wong A, Timofeyev V, Young JN, Majdi M, Li RA, Chen HS, Chiamvimonvat N. MicroRNA profiling predicts a variance in the proliferative potential of cardiac progenitor cells derived from neonatal and adult murine hearts. *J Mol Cell Cardiol.* 2012;52:264-272.
17. Lian X, Zhang J, Azarin SM, Zhu K, Hazeltine LB, Bao X, Hsiao C, Kamp TJ, Palecek SP. Directed cardiomyocyte differentiation from human pluripotent stem cells by modulating Wnt/beta-catenin signaling under fully defined conditions. *Nature Protocols.* 2013;8:162-175.
18. De Jesus NM, Wang L, Herren AW, Wang J, Shenasa F, Bers DM, Lindsey ML, Ripplinger CM. Atherosclerosis exacerbates arrhythmia following MI: Role of myocardial inflammation. *Heart Rhythm.* 2015;12:169-178.

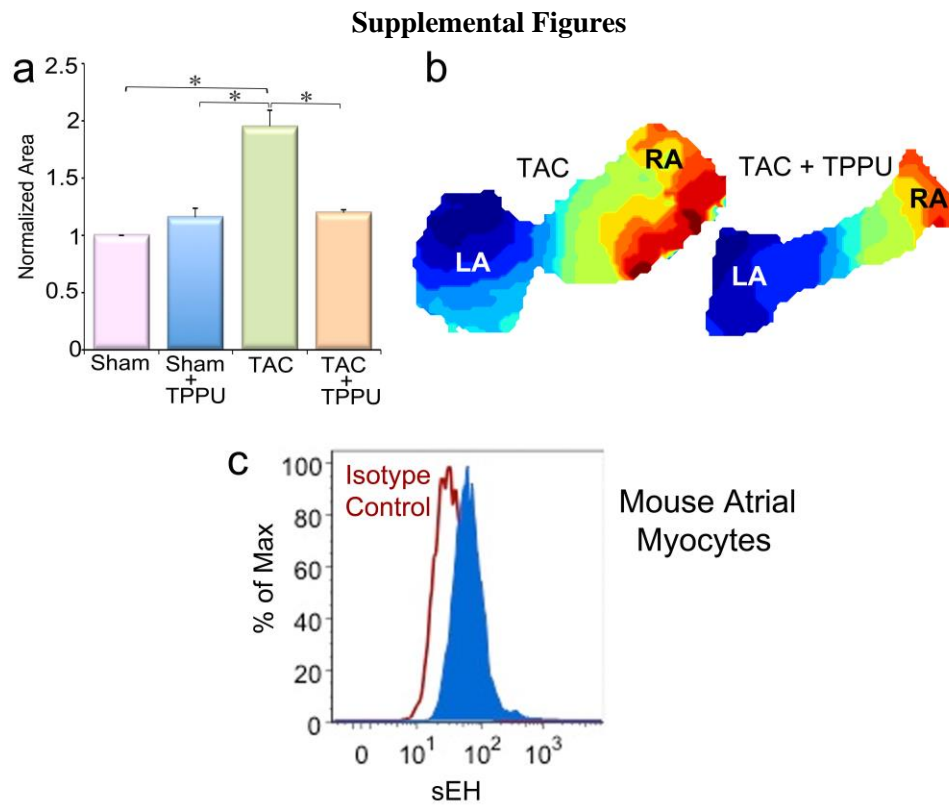


Figure I. Assessment of the effect of TPPU on cardiac dilatation: (a) Summary data of atrial area in sham-operated (pink), TPPU-treated sham-operated (blue), TAC (green), and TAC treated with TPPU (orange) after three weeks of TPPU treatment showing evidence of chamber dilatation in TAC mice. TPPU prevented the development of chamber dilatation in TAC mice. (b) Example maps of atria from TAC (left) and TPPU-treated-TAC (right) hearts. (c) Presence of sEH in atrial myocytes (blue) analyzed through flow cytometry. Mean±SEM. n=3, * $P < 0.05$

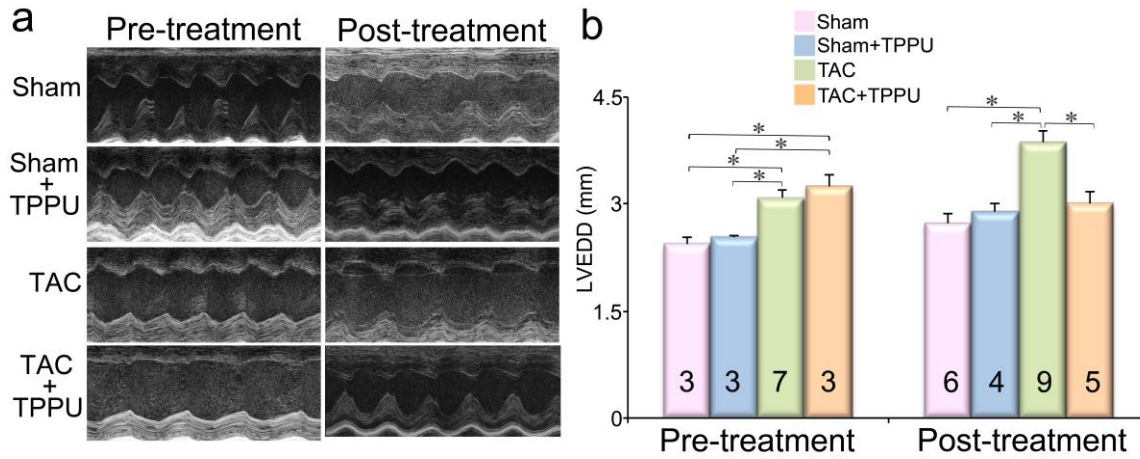


Figure II. Noninvasive echocardiographic assessment of the effect of TPPU on cardiac function: (a) Examples of two-dimensional and M-mode echocardiography in sham-operated (pink), TPPU-treated sham-operated (blue), TAC (green) and TAC treated with TPPU (orange) after three weeks of TPPU treatment showing evidence of chamber dilatation in TAC mice. TPPU prevented the development of chamber dilatation in TAC mice. **(b)** Summary data for left ventricular end diastolic dimension (mm) from the four groups of animals. Error bars represent standard error, numbers inside the graph represents n and * $P < 0.05$. ** $P < 0.05$ vs Sham and Sham+TPPU.

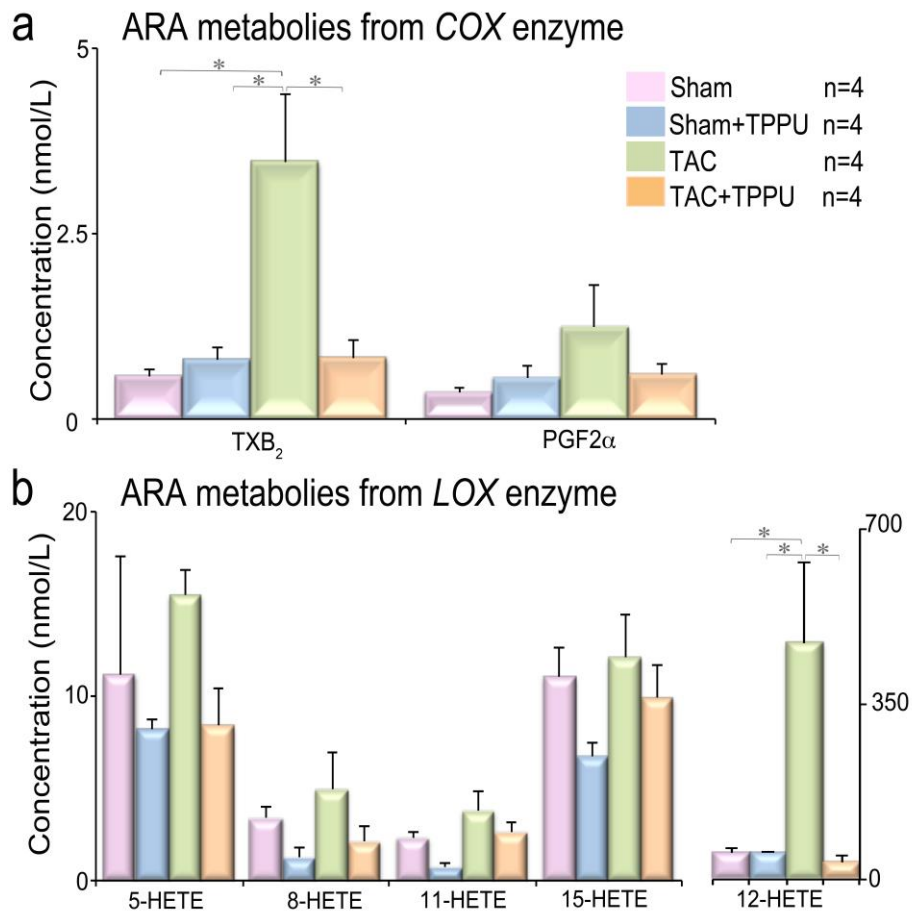


Figure III. Oxylin Profiling: (a) Oxylin profiling of arachidonic acid metabolites from *COX-2* enzyme from sham-operated (pink), TPPU-treated sham-operated (blue), TAC (green) and TAC treated with TPPU (orange) after three weeks of TPPU treatment. (b) Oxylin profiling of arachidonic acid metabolites from *LOX* enzyme. Error bars represent standard error and * $P < 0.05$.

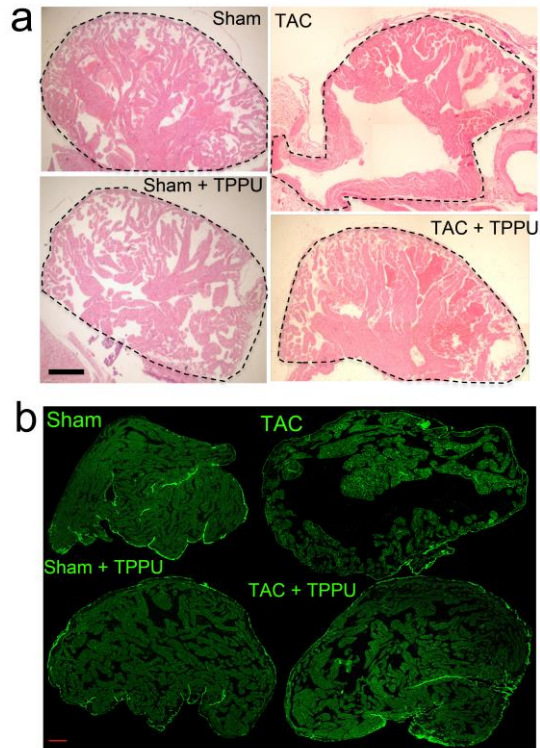


Figure IV. *TPPU reduces atrial fibrosis:* (a) Cardiac sections from right atria stained with Sirius Red demonstrate the amount of collagen deposition. Scale bars, 500 μm . (b) Confocal images of wheat germ agglutinin stain showing a significant decrease in collagen deposition in the TPPU-treated TAC mice compared to TAC alone in the right atria. Scale bars, 200 μm .

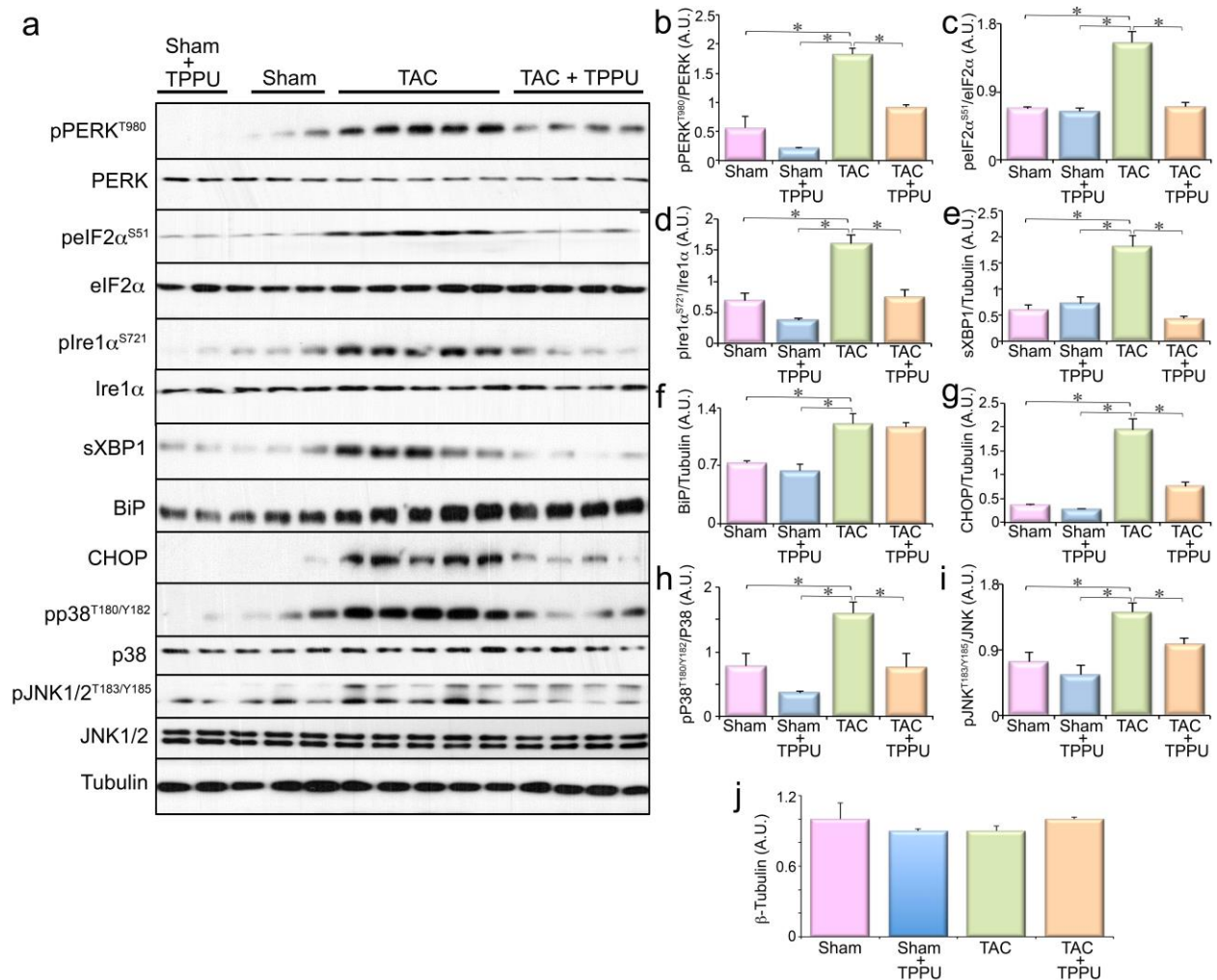


Figure V. ER Stress Assay from TAC and TPPU-treated TAC mice: (a) Total protein lysates were immunoblotted for pPERK, peIF2 α , pIRE1 α , pp38, pJNK1/2 and their respective unphosphorylated proteins, sXBP1, BiP, CHOP and Tubulin as a loading control. Bar graphs represent normalized data. (b) pPERK/PERK, (c) peIF2 α / eIF2 α , (d) pIRE1 α /IRE1 α , (e) sXBP1 normalized to Tubulin, (f) BiP normalized to β -Tubulin (g) CHOP normalized to Tubulin (h) pp38/p38, and (i) pJNK/JNK. (j) Levels of β -tubulin in the four groups of animals. AU: arbitrary units. Error bars represent standard error, and $*P < 0.05$. Sham-operated (pink bars), TPPU-treated-sham-operated (blue bars), TAC (green bars) and TPPU-treated-TAC mice (orange bars); n=3-5 animals.

Supplemental Tables

Table I: Oxylipin Profiling Data: Plasma levels of oxylipin mediators (nmol/L) and the ratios of epoxides to diols. Data Average \pm Standard Error.

Oxylipins	Treatment Groups			
	Sham	Sham+TPPU	TAC	TAC+TPPU
5(6)-EET	36.73 \pm 6.4	38.54 \pm 8.1	36.06 \pm 8.3	58.77 \pm 5.7
5(6)-DHET	2.39 \pm 0.4	0.91 \pm 0.2	2.03 \pm 0.1	0.93 \pm 0.1
8(9)-EET	4.19 \pm 0.6	5.02 \pm 1.2	3.91 \pm 0.78	7.41 \pm 0.6
8(9)-DHET	1.20 \pm 0.1	1.06 \pm 0.2	2.02 \pm 0.2	1 \pm 0.04
11(12)-EET	4.52 \pm 0.2	6.31 \pm 1.2	5.7 \pm 0.6	6.62 \pm 0.6
11(12)-DHET	0.43 \pm 0.05	0.30 \pm 0.03	0.61 \pm 0.1	0.36 \pm 0.04
14(15)-EET	2.06 \pm 0.3	5.5 \pm 1.7	2.67 \pm 0.2	6.10 \pm 1.6
14(15)-DHET	0.91 \pm 0.1	0.96 \pm 0.05	1.58 \pm 0.3	1.01 \pm 0.09
Sum EETs	47.50 \pm 7.3	55.37 \pm 11.5	48.34 \pm 9.4	78.92 \pm 7.13
Sum DHETs	2.54 \pm 0.3	2.32 \pm 0.2	4.22 \pm 0.5	2.37 \pm 0.1
Sum-EpOMEs	50.09 \pm 9.3	216 \pm 58	124 \pm 53	138 \pm 19
Sum-DiHOMEs	19.83 \pm 3.9	18 \pm 3	42 \pm 12	27 \pm 3.4
Sum-EpODEs	13.54 \pm 3.5	54.65 \pm 20	16.9 \pm 2.9	29.47 \pm 6.3
Sum-DiHODEs	7.59 \pm 1.1	3.73 \pm 1.1	10.81 \pm 1.5	2.92 \pm 0.3
Sum-EpDPEs	28.1 \pm 16	62.38 \pm 58	26.89 \pm 10	79.19 \pm 34
Sum-DiHDPEs	3.2 \pm 0.5	2.81 \pm 0.6	7.93 \pm 2.4	2.98 \pm 0.9
5(6)-EET/5(6)-DHET	16.15 \pm 2.4	61.28 \pm 22.2	17.17 \pm 3	64.9 \pm 7.8
8(9)-EET/8(9)-DHET	3.53 \pm 0.5	4.85 \pm 0.8	1.96 \pm 0.3	7.38 \pm 0.4
11(12)-EET/11(12)-DHET	11.23 \pm 1.6	21 \pm 2.9	11.49 \pm 3.2	19.18 \pm 3.07
14(15)-EET/14(15)-DHET	2.5 \pm 0.5	5.79 \pm 1.8	1.89 \pm 0.3	5.91 \pm 1.4
Sum(EETs)/Sum(DHETs)	19.28 \pm 3.2	24.13 \pm 4.4	13.43 \pm 5.9	33.42 \pm 2.7
Sum(EpOMEs)/Sum(DiHOMEs)	2.62 \pm 0.3	11.15 \pm 1.5	2.71 \pm 0.3	5.2 \pm 0.7
Sum(EpODEs)/Sum(DiHODEs)	11.69 \pm 1.5	33.9 \pm 8.7	5.87 \pm 1.3	15.08 \pm 1.45
Sum(EpDPEs)/Sum(DiHDPEs)	21.33 \pm 6.9	46.57 \pm 39	13.96 \pm 5.3	71.15 \pm 29

EET, epoxyeicosatrienoic acid; DHET, dihydroxyeicosatrienoic acid, EpOME, epoxyoctadecenoic acid; DiHOME, dihydroxyoctadecenoic acids; EpODE, epoxy-octadecadienoic acid; DiHODE, dihydroxy-octadecadienoic acid; EpDPE, epoxy-docosapentaenoic acid; DiHDPE, dihydroxy- docosapentaenoic acid

Table II: Plasma levels of Arachidonic Acid (ARA) metabolites (nmol/L) generated from COX-2 and LOX enzymes.

COX-2	Treatment Groups			
	Sham	Sham+ TPPU	TAC	TAC+ TPPU
TXB ₂	0.57±0.09	0.80±0.1	3.5±0.9	0.82±0.2
PGF2 α	0.36±0.07	0.55±0.1	1.24±0.5	0.6±0.1
LOX	Treatment Groups			
	Sham	Sham+ TPPU	TAC	TAC+ TPPU
5-HETE	11.2±2.2	8.2±0.5	15.5±1.3	8.4±2
8-HETE	3.4±0.6	1.2±0.6	5.0±1.9	2.1±0.7
11-HETE	2.3±0.3	0.7±0.2	3.8±1.0	2.6±0.5
12-HETE	53.4±10	53.8±2.4	472±161	34.3±12
15-HETE	11.0±1.6	6.7±0.7	12.1±2.3	9.93±1.7

TXB₂; Thromboxane 2, PGF2 α ; Prostaglandin F2 α , COX-2; Cyclooxygenase -2, LOX; Lipoxygenase, HETE; Hydroxyeicosatetraenoic acid

DATA SUPPLEMENT

Supplemental Materials and Methods

Soluble epoxide hydrolase inhibitor (sEHI):

Selective and potent inhibitors (low nanomolar K_i 's) for rodent and human sEH were developed based on the catalytic mechanism and the X-ray structure of the murine sEH (PDB access #: 1CQZ & 1CR6).¹⁻³ The potency, pharmacokinetics, and physicochemical properties of 11 different sEHIs were conducted. 1-Trifluoromethoxyphenyl-3-(1-propionylpiperidine-4-yl)urea (TPPU, containing a piperidine ring, Figure 1A) was found to have high inhibitory potency, drug-like physicochemical properties, pharmacokinetics with high area under the curve values, a relatively longer half-life and lower plasma protein binding properties than many previous compounds.⁴ For these pharmacokinetic favorable characteristics, TPPU was chosen for this study. TPPU was found to be a low nanomolar inhibitor of the sEH enzyme and was previously tested against commercial drug targets and the NIH screen of drug targets, there were no hits at 10 micromolar (over 1,000 fold higher concentration than the effective concentration for the sEH enzyme). In addition, the X-ray crystal structure of the soluble epoxide enzyme and the inhibitors has been solved.⁵⁻¹² There is no evidence to date of off-target binding sites.

Thoracic Aortic Constriction (TAC) model in mice:

TACs were performed in 8- to 12-week-old male C57BL/6J mice (Charles River, Wilmington, MA) as previously described.¹³ Mice from the same litters were used for sham, sham-TPPU treatment, TAC and TAC-TPPU treatment. Briefly, animals were anesthetized with i.p. ketamine 50 mg/kg and xylazine 2.5 mg/kg. Intubation was performed perorally and mechanical ventilation was initiated. Aortic constriction was created *via* a left thoracotomy by placing a ligature securely around the ascending aorta and a 26-gauge needle and then removing the needle. The chest was closed with 3-0 dextron rib sutures, 5-0 dextron II muscle sutures and buried skin sutures. Negative pleural pressure was re-established *via* a

temporary chest tube until spontaneous breathing occurs. Sham-operated animals underwent the same procedure without tying the suture. Echocardiograms were performed 1 week after surgery after which mice were randomized to receive TPPU (15 mg/L)¹⁴ in the drinking water or water alone for a period of 3 weeks. Four groups of animals including sham, sham treated with TPPU, TAC, and TAC treated with TPPU were followed for a period of three weeks at which time repeat echocardiograms were performed.

Analysis of cardiac function by echocardiography:

Echocardiograms to assess systolic function were performed by using M-mode and two-dimensional measurements as described previously.¹⁵ The measurements represented the average of six selected cardiac cycles from at least two separate scans performed in a blinded fashion with papillary muscles used as a point of reference for consistency in the level of scan. Fractional shortening (FS), a surrogate of systolic function, was calculated from left ventricle dimensions as follows: %FS = ((EDD-ESD)/EDD) x100, where EDD and ESD represent end-diastolic and end-systolic dimensions, respectively.

Histological analyses:

Hearts were excised and retrogradely perfused with phosphate-buffered solution to wash out blood and fixed in 10% formalin overnight. Hearts were then embedded in paraffin, serial left atrial (LA) and right atrial (RA) cardiac sections of 5 µm in thickness were taken along the longitudinal axis and stained with Picrosirius Red to assess for collagen content.

Immunofluorescence confocal laser scanning microscopy:

Additional cardiac sections were stained with wheat germ agglutinin (WGA). The cardiac sections were deparaffinized with Xylene before rehydrating with serial dilution of ethanol. The sections were blocked with donkey serum and stained with WGA-conjugated to Alexafluor-488 (10 µg ml⁻¹,

Molecular Probes). Cardiac sections from corresponding area from the four groups were scanned. Identical settings were used for all the specimens. Immunofluorescence-labeled images were obtained using a Zeiss LSM700 confocal laser-scanning microscope.

Flow cytometric analysis of cardiac cells:

Single cell suspension was obtained from 8- to 12-week-old male C57BL/6 mice as previously described.¹⁶ The procedure was performed according to the approved UC Davis Animal Care and Use protocol. Briefly, mice were injected with 0.1 ml heparin (1,000 units ml⁻¹) 10 min prior to heart excision, then anesthetized with pentobarbital intraperitoneally (80 mg kg⁻¹). Hearts were removed and placed in Tyrode's solution (mmol l⁻¹: NaCl 140, KCl 5.4, MgCl₂ 1.2, *N*-2-hydroxyethylpiperazine-*N'*-2-ethanesulphonic acid (HEPES) 5 and glucose 5, pH 7.4). All chemicals were obtained from Sigma Chemicals (St. Louis, MO) unless stated otherwise. The aorta was cannulated under a dissecting microscope and mounted on the Langendorff apparatus. The coronary arteries were retrogradely perfused with Tyrode's solution gassed with O₂ at 37 °C for 3 min at a flow rate of ~3 ml min⁻¹. The solution was switched to Tyrode's solution containing collagenase type 2 (1 mg ml⁻¹, 330 units mg⁻¹, Worthington Biochemical Corporation). After ~12 min of enzyme perfusion, hearts were removed from the perfusion apparatus and gently teased in high-K⁺ solution (mmol l⁻¹: potassium glutamate 120, KCl 20, MgCl₂ 1, EGTA 0.3, glucose 10 and HEPES 10, pH 7.4 with KOH). Cells were filtered through 200 µm cell strainer, re-suspended in Ca²⁺ and Mg²⁺ free phosphate buffered saline (PBS), fixed with 0.4% paraformaldehyde (PFA), treated with methanol before treating with phytoerythrin-conjugated anti-Thy1.2 (BD Bioscience, San Diego, CA), lineage antibody cocktail (CD3e, CD11b, Cd45R, Ly-6C, Ly-6G and TER-119, 1:100 dilution, BD Bioscience), anti-CD45 (BD Bioscience, San Diego, CA), anti-troponin T antibody (Thermo Scientific), anti-CD31 (BD Bioscience), Alexa fluor 488 or 647-conjugated anti-pERK1/2 (Cell Signaling), Alexa fluor 647-conjugated anti-pSMAD2/3 (BD Bioscience), and proliferation-specific Ki67 antibody (15 µg ml⁻¹, BD Bioscience) in PBS with 5% donkey serum and 20 µg ml⁻¹ DNase-free RNase (Sigma) overnight at 4°C. Cells were also stained with 40 µg ml⁻¹ 7-amino-

actinomycin D (7AAD, BD Bioscience, San Jose, CA) to measure the DNA content. Equal number of atrial myocytes (left and right together) were isolated from sham, sham-TPPU treated, TAC and TAC-TPPU treated hearts and 10,000 to 20,000 cells were analyzed in each run. Data were collected using a standard FACScan cytometer (BD Biosciences, San Jose, CA) upgraded to a dual laser system with the addition of a blue laser (15 mW at 488 nm) and a red laser (25 mW at 637 nm Cyttek Development, Inc, Fremont, CA). Data were acquired using CellQuest software (BD Bioscience) and analyzed using FlowJo software (ver9.4 Treestar Inc., San Carlos). Cells stained with isotype-matched IgG antibodies were used as controls to determine the positive cell population.

In vitro human cardiac fibroblast culture:

Human right atrial appendage specimens from informed consented patients undergoing cardiac bypass surgery were obtained from UC Davis Medical Center in accordance with the approved UC Davis Institutional Review Board (IRB) protocol. The tissue was stored in cardioplegic solution at 4°C and processed within 2 hours. The cardiac tissue was washed and minced in filter-sterilized (0.2 µm) Ca²⁺-and bicarbonate-free Hanks' buffer with HEPES (CBFHH) solution (mmol l⁻¹: NaCl 137, KCl 5.36, MgSO₄ 0.81, HEPES 20.06, K₂PO₄ 0.44, and Na₂HPO₄ 0.34, pH 7.4) at room temperature. The tissue pieces were digested with CBFHH solution containing 2% bovine serum albumin, 0.1% collagenase type 2 and 0.2% trypsin with continuous stirring at 37°C for 3 min. The supernatant was discarded and the enzyme solution replaced for 10 min and repeated for 3 min. The partially dissociated pieces were washed with medium before plating on cell culture dishes and maintained in DMEM/F12 medium (10% fetal bovine serum and 1% penicillin/streptomycin) until the appearance of fibroblasts from the explants. The cells were trypsinized and plated on 12 well plates until confluency and treated with angiotensin II (Sigma and 1 µM for 24 hours) and TPPU (1 µM) before flow cytometric analysis with phytoerythrin-conjugated anti-Thy1.1 (BD Bioscience, San Diego, CA), FITC conjugated lineage antibody cocktail (CD3, CD14, CD19, CD20 and CD56 BD Bioscience), APC-Cy7-conjugated anti-CD45 (BD Bioscience, San Diego, CA) and proliferation-specific Ki67 antibody (15 µg ml⁻¹, BD Bioscience).

Human-induced pluripotent stem cell-derived cardiomyocytes (hiPSC-CM) and hiPSC-derived cardiac fibroblasts:

HiPSC were plated and differentiated for 20 days using a directed differentiation protocol.¹⁷ HiPSC-CMs enriched with puromycin and treated with Tumor Necrosis Factor- α (TNF- α) or angiotensin II (ANG II) and TPPU were fixed and stained with anti- α -actinin, anti-NF- κ B, anti-myosin light chain-2a (MLC2a), anti- myosin light chain-2v (MLC2v) and fibroblast-specific antibodies. HiPSC-derived cardiac fibroblasts were defined as Thy1.1⁺/Lin⁻/CD45⁻ cells (hiPSC-Thy^{pos} cells). Differentiated hiPSCs at day 20 were treated with angiotensin II (Sigma and 1 μ M for 24 hours) or TNF- α (20 ng/ml for 20 minutes) and TPPU (1 μ M) before flow cytometric analyses as described above.

Western Blot Analysis:

Immunoblots were performed as previously described¹⁶ using anti-I κ B (1:1000, Cell Signaling), anti-phospho-I κ B (1:1000, Cell Signaling), anti-NF- κ B (1:1000, Cell Signaling) and anti-GAPDH (1:10000, Fitzgerald) antibodies.

Measurement of Plasma Cytokine Levels:

Plasma samples were collected 3 weeks after sham or TAC operation and stored at -80 °C until assayed. Plasma cytokine levels were analyzed using a Cytometric Bead Array kit (CBA mouse inflammation kit, BD Biosciences). Briefly, thawed plasma samples were mixed for 2 hours at room temperature with fluorescence-labeled capture beads with the PE detection reagents to measure the concentrations of Interleukin-6 (IL-6), Interleukin-10 (IL-10), Monocyte Chemoattractant Protein-1 (MCP-1), Interferon- γ (INF- γ), Tumor necrosis factor- α (TNF- α), and Interleukin-12p70 (IL-12 p70). Samples were then washed with washing buffer and analyzed on a FACScan flow cytometer (BD Immunocytometry Systems). Data were analyzed using BD Cytometric Bead Array Analysis software (BD Immunocytometry Systems).

Metabolomic Profiling of Oxylipins:

Plasma samples stored at -80 °C were thawed at room temperature. Aliquots of plasma (200 µL) were spiked with a set of odd chain length analogs and deuterated isomers of several target analytes including hydroxyeicosatetraenoic acids (HETEs), prostaglandins, thromboxanes, epoxides (EpOMEs and EETs), and diols (DHOMEs and DHETs) contained in 10 µL of methanol, and then were extracted by solid phase extraction using Oasis HLB cartridges (Waters, Milford, MA). The HLB columns (1 cc, 60 mg) were washed with 2 mL methanol and pre-conditioned with 2 mL water/methanol/acetic acid (95/5/0.1, v/v). Samples were then mixed with 200 µL of the pre-conditioning solution and loaded onto the column. The loaded column was then washed with 2 mL of the pre-conditioning solution and then dried for 5 min *in vacuo*. Target analytes were then eluted with 2 mL of ethyl acetate. The collected eluents were evaporated to dryness using a centrifugal vacuum concentrator and re-dissolved in 40 µL of methanol. The spiked samples were vortexed for 1 min, centrifuged at 14,000 r.p.m. for 5 min, and then transferred to analytical vials containing 150 µL inserts for analysis.

The oxylipin profiling was performed using a previously published method.¹³ The separation of plasma oxylipins was conducted in a Shimadzu LC-10AD_{VP} instrument (Shimadzu Corp., Kyoto, Japan) equipped with a 2.1 mm X 150 mm Pursuit XR_S-C18 5 µm column (Varian Inc, Palo Alto, CA) held at 40 °C. A gradient of water containing 0.1% acetic acid (v/v, solvent A) and acetonitrile/methanol/acetic acid (800/150/1, v/v; solvent B) was used to elute the column with the flow rate of 0.4 mL min⁻¹ (SI Table 1). The injection volume was 10 µL and the samples were kept at 10 °C in the auto sampler. Analytes were detected on a 4000 QTRAP (Applied Biosystems, Foster City, CA) hybrid, triple-quadrupole, and linear ion trap mass spectrometer equipped with a Turbo V ion source and operated in negative MRM mode. The source was operated in negative electrospray mode and the QTRAP was set as follows: CUR=20 psi, GS1=50 psi, GS2=30 psi, IS=-4500 V, CAD= HIGH, TEM=400°C, ihe=ON, DP=-60 V. The collision energies used for CAD ranged from -18 to -38 eV.

Evaluation of Endoplasmic Reticulum (ER) Stress markers:

Atrial tissues were homogenized in RIPA buffer supplemented with protease inhibitors and phosphatase inhibitors (10 mM Tris-HCl, pH 7.4, 150 mM NaCl, 0.1% sodium dodecyl sulfate, 1% TritonX-100, 1% sodium deoxycholate, 5 mM EDTA, 1 mM NaF, 1 mM sodium orthovanadate and protease inhibitors). Lysates were clarified by centrifugation at 13,000 rpm for 10 min and protein concentrations were determined using bicinchoninic acid protein assay kit (Pierce Chemical). Proteins were resolved by SDS-PAGE and transferred to PVDF membranes. Immunoblotting of lysates was performed with antibodies for pp38 (Thr180/Tyr182), p38, pJNK (Thr183/Tyr185), JNK, (Cell Signaling Technology; Danvers, MA), pPERK (Thr980), PERK, pEIF2 α (Ser51), eIF2 α , sXBP1, IRE1 α and Tubulin (all from Santa Cruz Biotechnology; Santa Cruz, CA). Antibody for pIRE1 α (Ser724) was obtained from Abcam, Cambridge, MA. After incubation with the appropriate secondary antibodies, proteins were visualized using enhanced chemiluminescence (ECL, Amersham Biosciences). Pixel intensities of immunoreactive bands were quantified using ImageQuant 5.0 software (Molecular Dynamics). Data for phosphorylated proteins are presented as phosphorylation level normalized to total protein expression and for non-phosphorylated proteins as total protein expression normalized to β -tubulin, which remains unchanged in the four groups. **Fig S5j**).

Ex vivo Optical Mapping of transmembrane potential (V_m):

Langendorff perfusion and optical mapping of V_m were carried out as described previously.¹⁸ Briefly, mice were anesthetized with pentobarbital sodium (150 mg/kg, I.P.) containing 120 IU of heparin. Following a mid-sternal incision, hearts were rapidly removed and perfused in a 37 \pm 0.5 $^{\circ}$ C Tyrode's solution of the following composition (in mmol/L): NaCl 128.2, CaCl₂ 1.3, KCl 4.7, MgCl₂ 1.05, NaH₂PO₄ 1.19, NaHCO₃ 20 and glucose 11.1 (pH 7.4 \pm 0.05). Flow rate (1.5-3.5 mL/min) was adjusted to maintain a perfusion pressure of 60-80 mmHg. The hearts were placed in a perfusion dish with the posterior surface of the heart facing the optical mapping camera. In addition to coronary perfusion, the hearts were submerged in the solution and superfused in the dish to keep the temperature at 37 \pm 0.5 $^{\circ}$ C.

The atrial appendages were pinned in the dish with fine insect pins to elevate the posterior epicardium of the atrial appendages into the focal plane for imaging. A bipolar pacing electrode was positioned on the epicardium of left or right atrial appendage for pacing using a 2 ms pulse at twice the diastolic threshold. Blebbistatin (10-20 μ M, Tocris Bioscience, Ellisville, MO) was added to the perfusate to reduce motion artifacts during optical recordings (Fedorov VV et al., Heart Rhythm, 2007). The heart was stained with the voltage-sensitive dye (RH237, 5 μ L of 1 mg/mL in DMSO, Molecular Probes) via the coronary perfusion. Excitation light was produced with two continuous-wave LED sources centered at 531 nm and bandpass filtered from 511-551 nm (LEX-2, SciMedia, Costa Mesa, CA). The emitted fluorescence was collected through an objective (Leica, 1x) and the fluorescence signal longpass filtered at 700 nm. Optical action potentials were recorded using a 16-bit complementary metal oxide camera (CMOS, MiCam Ultima-L, SciMedia, Costa Mesa, CA). Images were acquired at 1 kHz and 100x100 pixels with a 10x10 mm field of view.

Baseline electrophysiological parameters were determined during atrial epicardial pacing at a pacing cycle length (PCL) of 100 ms. Effective refractory period (ERP) was determined using a standard S1-S2 pacing protocol (18 S1s at 100ms followed by a premature S2 stimulus decreasing by 5-10 ms until the ERP was reached). ERP was measured from both the left and right atrium. Data analysis was performed using a commercially available analysis program (*Optiq*, Cairn, UK). The V_m signals were post-processed using a spatial Gaussian filter (3x3 pixels). Action potential (AP) characteristics were analyzed from data collected during pacing at a PCL of 100 ms from the left appendage. AP activation time was determined as the time at 50% between peak and baseline amplitude. Action potential duration at 80% repolarization (APD_{80}) was calculated as repolarization time – activation time from data collected during pacing at 100 ms (S1) or 60 ms (S2) on the left or right atrial appendage. Pseudo-color AP activation and APD_{80} maps were generated from measurements of activation time and APD_{80} at individual pixels. The sizes and shapes of the maps were selected based on the signal-to-noise ratio levels of the mapping area that allow for proper analysis.

Electrophysiological studies of single isolated atrial myocytes:

Atrial myocytes were isolated from hearts using previously described protocol.¹⁵ Briefly, hearts were removed, and retrogradely perfused with collagenase B (Boehringer Mannheim) and 3 mg protease (type XIV, 4.5 units/mg, Sigma). Experiments were performed using the conventional whole-cell patch-clamp technique at room temperature.¹⁵ For K⁺ current recording, the external solution contained (mM) NMG 130, KCl 5, CaCl₂ 1, MgCl₂ 1, Nimodipine 1 μM, glucose 10, HEPES 10, pH 7.4 with HCl. The pipette solution contained (mM) KCl 140, Mg-ATP 4, MgCl₂ 1, EGTA 10, HEPES 10, pH 7.4 with KOH. All experiments were performed using 3 M KCl agar bridges. Cell capacitance was calculated as the ratio of total charge (the integrated area under the current transient) to the magnitude of the pulse (20 mV). Currents were normalized to cell capacity to obtain the current density. The series resistance was compensated electronically. In all experiments, a series resistance compensation of 90% was obtained. Currents were recorded using Axopatch 200B amplifier (Axon 7 Instrument), filtered at 10 kHz using a 4-pole Bessel filter and digitized at sampling frequency of 50 kHz. Data analysis was carried out using custom-written software and commercially available PC-based spreadsheet and graphics software (MicroCal Origin version 6.0).

Statistical Analysis:

Data are presented as mean ± S.E.M. Statistical comparisons were analyzed by one-way ANOVA followed by Bonferroni tests and Tukey's-Kramer honest significant difference analyses for post hoc comparison. Statistical significance was considered to be achieved when $p < 0.05$ and $p < 0.01$ (for ER Stress assay).

Supplemental References

1. Argiriadi MA, Morisseau C, Goodrow MH, Dowdy DL, Hammock BD, Christianson DW. Binding of alkylurea inhibitors to epoxide hydrolase implicates active site tyrosines in substrate activation. *J Biol Chem.* 2000;275:15265-15270.
2. Argiriadi MA, Morisseau C, Hammock BD, Christianson DW. Detoxification of environmental mutagens and carcinogens: structure, mechanism, and evolution of liver epoxide hydrolase. *Proc Natl Acad Sci U S A.* 1999;96:10637-10642.
3. Morisseau C, Goodrow MH, Dowdy D, Zheng J, Greene JF, Sanborn JR, Hammock BD. Potent urea and carbamate inhibitors of soluble epoxide hydrolases. *Proc Natl Acad Sci U S A.* 1999;96:8849-8854.
4. Ulu A, Appt S, Morisseau C, Hwang SH, Jones PD, Rose TE, Dong H, Lango J, Yang J, Tsai HJ, Miyabe C, Fortenbach C, Adams MR, Hammock BD. Pharmacokinetics and in vivo potency of soluble epoxide hydrolase inhibitors in cynomolgus monkeys. *Br J Pharmacol.* 2012;165:1401-1412.
5. Gomez GA, Morisseau C, Hammock BD, Christianson DW. Structure of human epoxide hydrolase reveals mechanistic inferences on bifunctional catalysis in epoxide and phosphate ester hydrolysis. *Biochemistry.* 2004;43:4716-4723.
6. Gomez GA, Morisseau C, Hammock BD, Christianson DW. Human soluble epoxide hydrolase: structural basis of inhibition by 4-(3-cyclohexylureido)-carboxylic acids. *Protein Science.* 2006;15:58-64.
7. Garriga M, Caballero J. Insights into the structure of urea-like compounds as inhibitors of the juvenile hormone epoxide hydrolase (JHEH) of the tobacco hornworm *Manduca sexta*: analysis of the binding modes and structure-activity relationships of the inhibitors by docking and CoMFA calculations. *Chemosphere.* 2011;82:1604-1613.

8. Xing L, McDonald JJ, Kolodziej SA, Kurumbail RG, Williams JM, Warren CJ, O'Neal JM, Skepner JE, Roberds SL. Discovery of potent inhibitors of soluble epoxide hydrolase by combinatorial library design and structure-based virtual screening. *J Med Chem.* 2011;54:1211-1222.
9. Moser D, Achenbach J, Klingler FM, Estel la B, Hahn S, Proschak E. Evaluation of structure-derived pharmacophore of soluble epoxide hydrolase inhibitors by virtual screening. *Bioorganic Medicinal Chem Lett.* 2012;22:6762-6765.
10. Amano Y, Yamaguchi T, Tanabe E. Structural insights into binding of inhibitors to soluble epoxide hydrolase gained by fragment screening and X-ray crystallography. *Bioorganic Medicinal Chem.* 2014;22:2427-2434.
11. Takai K, Chiyo N, Nakajima T, Nariai T, Ishikawa C, Nakatani S, Ikeno A, Yamamoto S, Sone T. Three-dimensional rational approach to the discovery of potent substituted cyclopropyl urea soluble epoxide hydrolase inhibitors. *Bioorganic Medicinal Chem Lett.* 2015;25:1705-1708.
12. Amano Y, Tanabe E, Yamaguchi T. Identification of N-ethylmethylanine as a novel scaffold for inhibitors of soluble epoxide hydrolase by crystallographic fragment screening. *Bioorganic Medicinal Chem.* 2015;23:2310-2317.
13. Sirish P, Li N, Liu JY, Lee KS, Hwang SH, Qiu H, Zhao C, Ma SM, Lopez JE, Hammock BD, Chiamvimonvat N. Unique mechanistic insights into the beneficial effects of soluble epoxide hydrolase inhibitors in the prevention of cardiac fibrosis. *Proc Natl Acad Sci U S A.* 2013;110:5618-5623.
14. Hwang SH, Tsai HJ, Liu JY, Morisseau C, Hammock BD. Orally bioavailable potent soluble epoxide hydrolase inhibitors. *J Med Chem.* 2007;50:3825-3840.
15. Li N, Liu JY, Timofeyev V, Qiu H, Hwang SH, Tuteja D, Lu L, Yang J, Mochida H, Low R, Hammock BD, Chiamvimonvat N. Beneficial effects of soluble epoxide hydrolase inhibitors in myocardial infarction model: Insight gained using metabolomic approaches. *J Mol Cell Cardiol.* 2009;47:835-845.

16. Sirish P, Lopez JE, Li N, Wong A, Timofeyev V, Young JN, Majdi M, Li RA, Chen HS, Chiamvimonvat N. MicroRNA profiling predicts a variance in the proliferative potential of cardiac progenitor cells derived from neonatal and adult murine hearts. *J Mol Cell Cardiol.* 2012;52:264-272.
17. Lian X, Zhang J, Azarin SM, Zhu K, Hazeltine LB, Bao X, Hsiao C, Kamp TJ, Palecek SP. Directed cardiomyocyte differentiation from human pluripotent stem cells by modulating Wnt/beta-catenin signaling under fully defined conditions. *Nature Protocols.* 2013;8:162-175.
18. De Jesus NM, Wang L, Herren AW, Wang J, Shenasa F, Bers DM, Lindsey ML, Ripplinger CM. Atherosclerosis exacerbates arrhythmia following MI: Role of myocardial inflammation. *Heart Rhythm.* 2015;12:169-178.

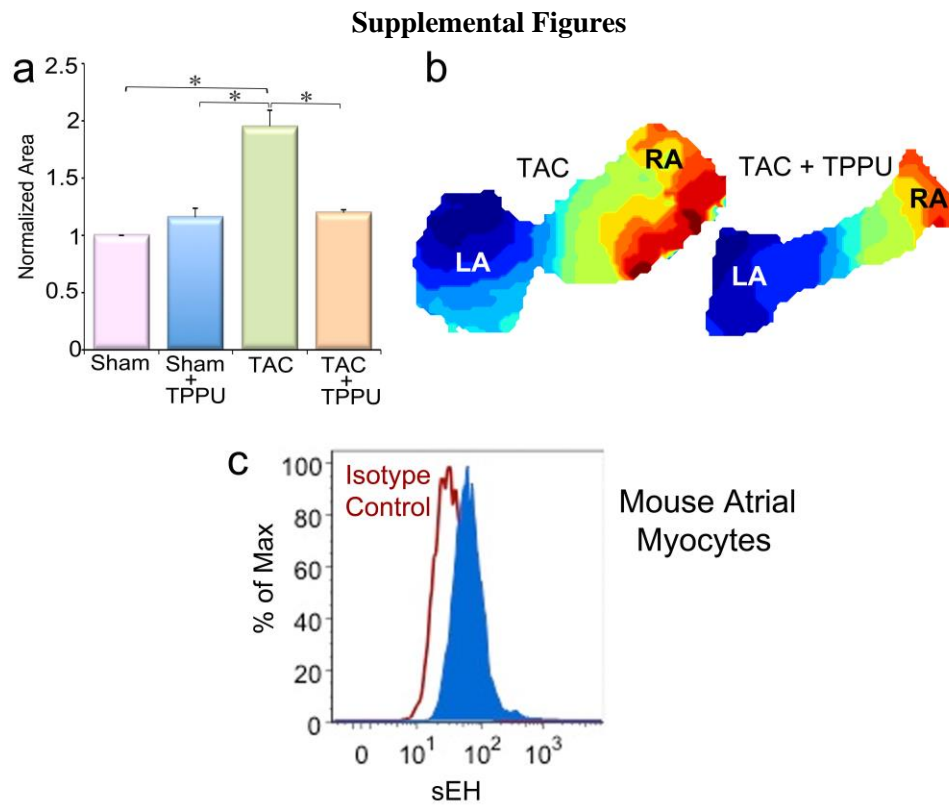


Figure I. Assessment of the effect of TPPU on cardiac dilatation: (a) Summary data of atrial area in sham-operated (pink), TPPU-treated sham-operated (blue), TAC (green), and TAC treated with TPPU (orange) after three weeks of TPPU treatment showing evidence of chamber dilatation in TAC mice. TPPU prevented the development of chamber dilatation in TAC mice. (b) Example maps of atria from TAC (left) and TPPU-treated-TAC (right) hearts. (c) Presence of sEH in atrial myocytes (blue) analyzed through flow cytometry. Mean±SEM. n=3, * $P < 0.05$

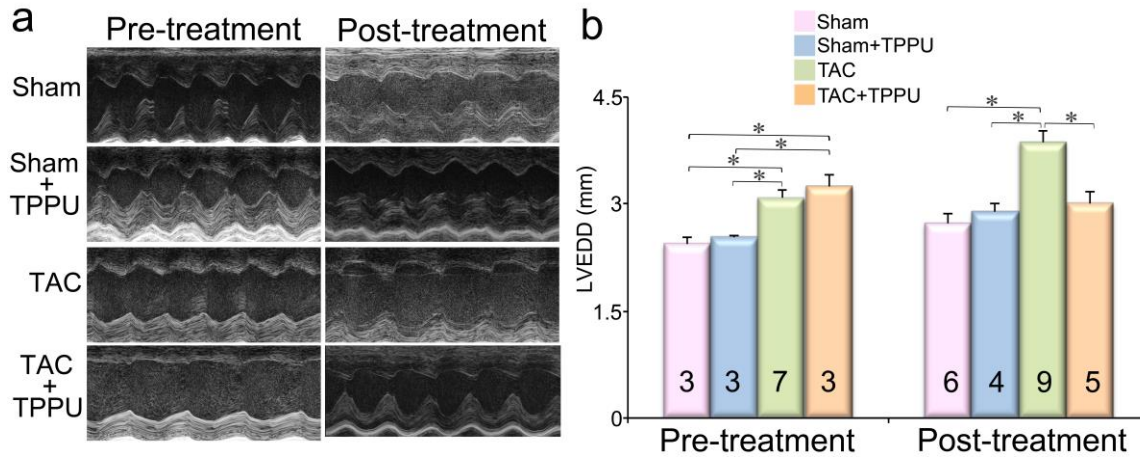


Figure II. Noninvasive echocardiographic assessment of the effect of TPPU on cardiac function: (a) Examples of two-dimensional and M-mode echocardiography in sham-operated (pink), TPPU-treated sham-operated (blue), TAC (green) and TAC treated with TPPU (orange) after three weeks of TPPU treatment showing evidence of chamber dilatation in TAC mice. TPPU prevented the development of chamber dilatation in TAC mice. **(b)** Summary data for left ventricular end diastolic dimension (mm) from the four groups of animals. Error bars represent standard error, numbers inside the graph represents n and * $P < 0.05$. ** $P < 0.05$ vs Sham and Sham+TPPU.

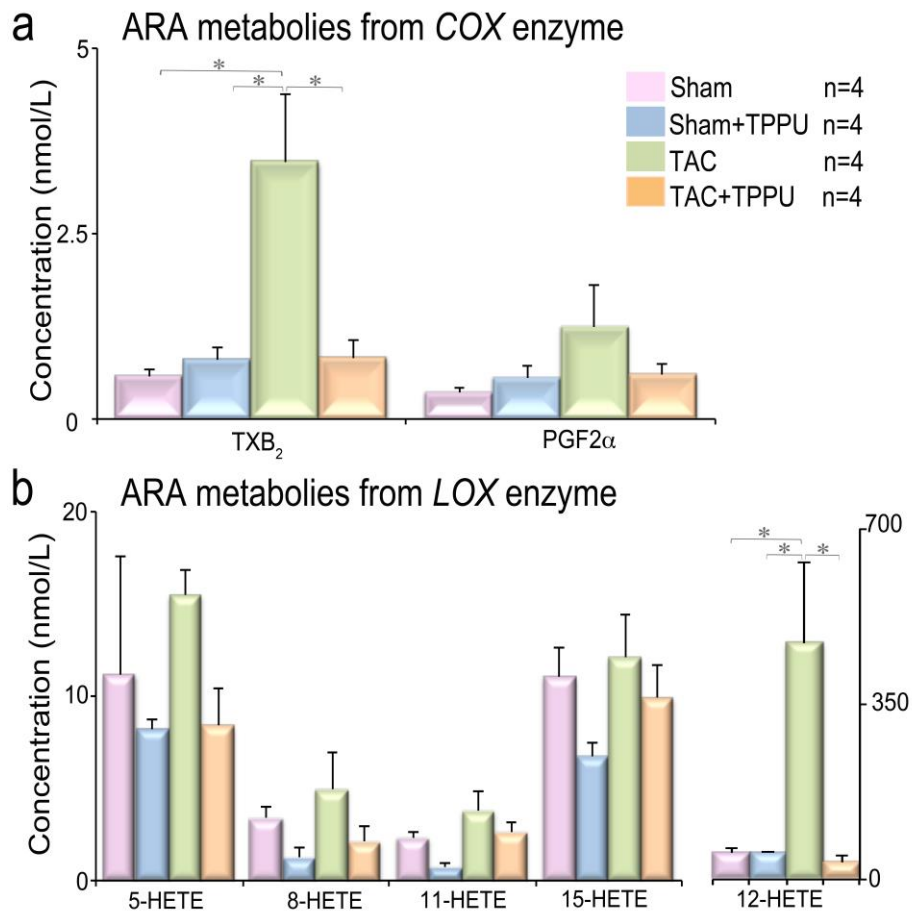


Figure III. Oxylin Profiling: (a) Oxylin profiling of arachidonic acid metabolites from *COX-2* enzyme from sham-operated (pink), TPPU-treated sham-operated (blue), TAC (green) and TAC treated with TPPU (orange) after three weeks of TPPU treatment. (b) Oxylin profiling of arachidonic acid metabolites from *LOX* enzyme. Error bars represent standard error and * $P < 0.05$.

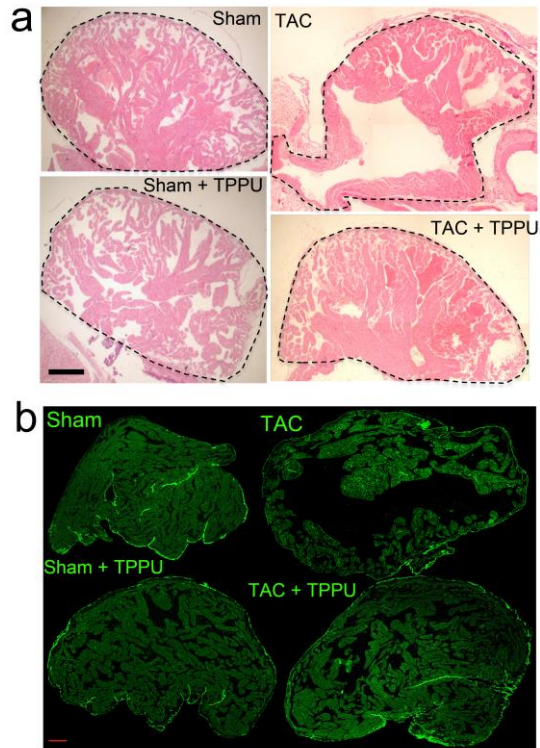


Figure IV. *TPPU reduces atrial fibrosis:* (a) Cardiac sections from right atria stained with Sirius Red demonstrate the amount of collagen deposition. Scale bars, 500 μm . (b) Confocal images of wheat germ agglutinin stain showing a significant decrease in collagen deposition in the TPPU-treated TAC mice compared to TAC alone in the right atria. Scale bars, 200 μm .

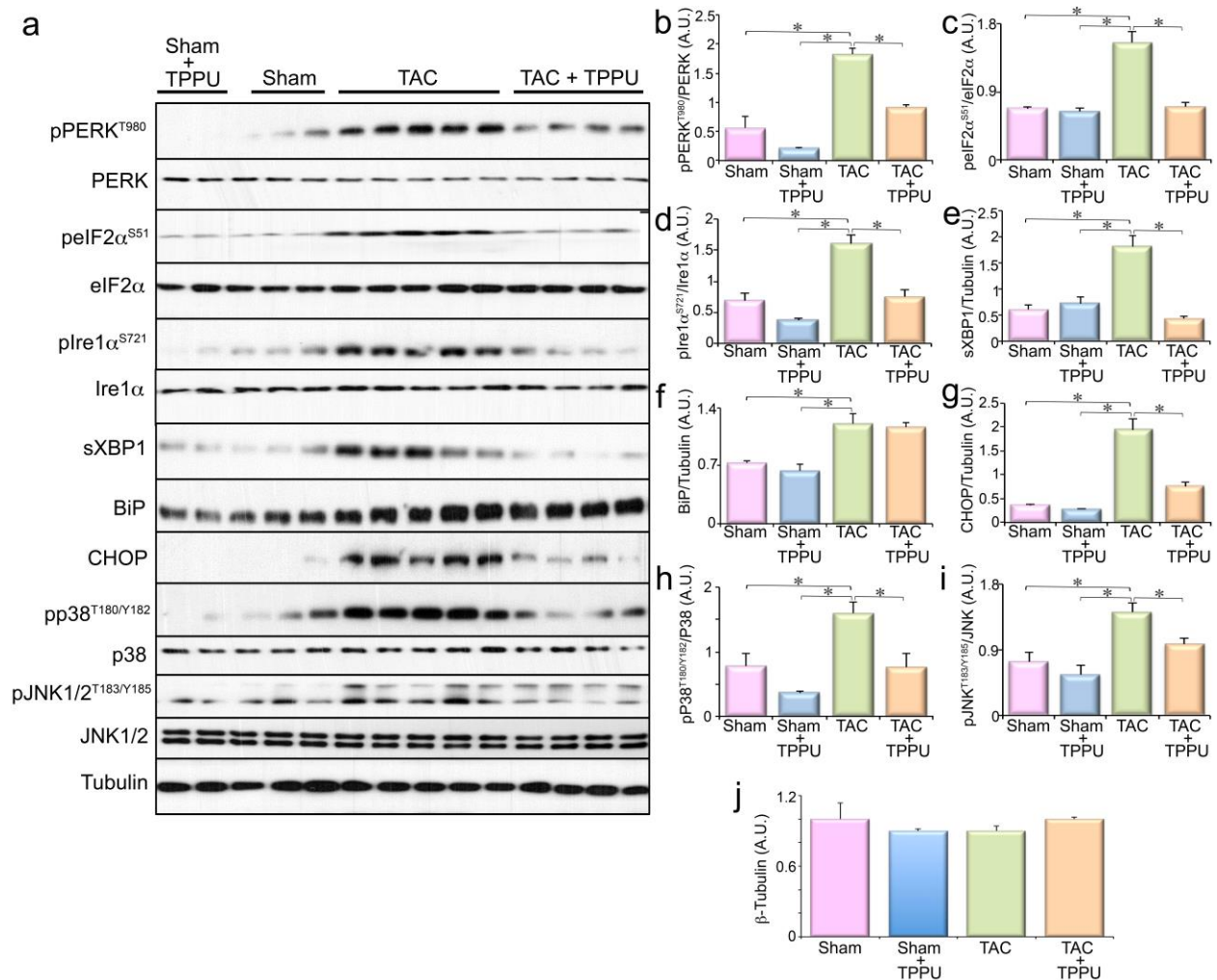


Figure V. ER Stress Assay from TAC and TPPU-treated TAC mice: (a) Total protein lysates were immunoblotted for pPERK, peIF2 α , pIRE1 α , pp38, pJNK1/2 and their respective unphosphorylated proteins, sXBP1, BiP, CHOP and Tubulin as a loading control. Bar graphs represent normalized data. (b) pPERK/PERK, (c) peIF2 α / eIF2 α , (d) pIRE1 α /IRE1 α , (e) sXBP1 normalized to Tubulin, (f) BiP normalized to β -Tubulin (g) CHOP normalized to Tubulin (h) pp38/p38, and (i) pJNK/JNK. (j) Levels of β -tubulin in the four groups of animals. AU: arbitrary units. Error bars represent standard error, and $*P < 0.05$. Sham-operated (pink bars), TPPU-treated-sham-operated (blue bars), TAC (green bars) and TPPU-treated-TAC mice (orange bars); n=3-5 animals.

Supplemental Tables

Table I: Oxylipin Profiling Data: Plasma levels of oxylipin mediators (nmol/L) and the ratios of epoxides to diols. Data Average \pm Standard Error.

Oxylipins	Treatment Groups			
	Sham	Sham+TPPU	TAC	TAC+TPPU
5(6)-EET	36.73 \pm 6.4	38.54 \pm 8.1	36.06 \pm 8.3	58.77 \pm 5.7
5(6)-DHET	2.39 \pm 0.4	0.91 \pm 0.2	2.03 \pm 0.1	0.93 \pm 0.1
8(9)-EET	4.19 \pm 0.6	5.02 \pm 1.2	3.91 \pm 0.78	7.41 \pm 0.6
8(9)-DHET	1.20 \pm 0.1	1.06 \pm 0.2	2.02 \pm 0.2	1 \pm 0.04
11(12)-EET	4.52 \pm 0.2	6.31 \pm 1.2	5.7 \pm 0.6	6.62 \pm 0.6
11(12)-DHET	0.43 \pm 0.05	0.30 \pm 0.03	0.61 \pm 0.1	0.36 \pm 0.04
14(15)-EET	2.06 \pm 0.3	5.5 \pm 1.7	2.67 \pm 0.2	6.10 \pm 1.6
14(15)-DHET	0.91 \pm 0.1	0.96 \pm 0.05	1.58 \pm 0.3	1.01 \pm 0.09
Sum EETs	47.50 \pm 7.3	55.37 \pm 11.5	48.34 \pm 9.4	78.92 \pm 7.13
Sum DHETs	2.54 \pm 0.3	2.32 \pm 0.2	4.22 \pm 0.5	2.37 \pm 0.1
Sum-EpOMEs	50.09 \pm 9.3	216 \pm 58	124 \pm 53	138 \pm 19
Sum-DiHOMEs	19.83 \pm 3.9	18 \pm 3	42 \pm 12	27 \pm 3.4
Sum-EpODEs	13.54 \pm 3.5	54.65 \pm 20	16.9 \pm 2.9	29.47 \pm 6.3
Sum-DiHODEs	7.59 \pm 1.1	3.73 \pm 1.1	10.81 \pm 1.5	2.92 \pm 0.3
Sum-EpDPEs	28.1 \pm 16	62.38 \pm 58	26.89 \pm 10	79.19 \pm 34
Sum-DiHDPEs	3.2 \pm 0.5	2.81 \pm 0.6	7.93 \pm 2.4	2.98 \pm 0.9
5(6)-EET/5(6)-DHET	16.15 \pm 2.4	61.28 \pm 22.2	17.17 \pm 3	64.9 \pm 7.8
8(9)-EET/8(9)-DHET	3.53 \pm 0.5	4.85 \pm 0.8	1.96 \pm 0.3	7.38 \pm 0.4
11(12)-EET/11(12)-DHET	11.23 \pm 1.6	21 \pm 2.9	11.49 \pm 3.2	19.18 \pm 3.07
14(15)-EET/14(15)-DHET	2.5 \pm 0.5	5.79 \pm 1.8	1.89 \pm 0.3	5.91 \pm 1.4
Sum(EETs)/Sum(DHETs)	19.28 \pm 3.2	24.13 \pm 4.4	13.43 \pm 5.9	33.42 \pm 2.7
Sum(EpOMEs)/Sum(DiHOMEs)	2.62 \pm 0.3	11.15 \pm 1.5	2.71 \pm 0.3	5.2 \pm 0.7
Sum(EpODEs)/Sum(DiHODEs)	11.69 \pm 1.5	33.9 \pm 8.7	5.87 \pm 1.3	15.08 \pm 1.45
Sum(EpDPEs)/Sum(DiHDPEs)	21.33 \pm 6.9	46.57 \pm 39	13.96 \pm 5.3	71.15 \pm 29

EET, epoxyeicosatrienoic acid; DHET, dihydroxyeicosatrienoic acid, EpOME, epoxyoctadecenoic acid; DiHOME, dihydroxyoctadecenoic acids; EpODE, epoxy-octadecadienoic acid; DiHODE, dihydroxy-octadecadienoic acid; EpDPE, epoxy-docosapentaenoic acid; DiHDPE, dihydroxy- docosapentaenoic acid

Table II: Plasma levels of Arachidonic Acid (ARA) metabolites (nmol/L) generated from COX-2 and LOX enzymes.

COX-2	Treatment Groups			
	Sham	Sham+ TPPU	TAC	TAC+ TPPU
TXB ₂	0.57±0.09	0.80±0.1	3.5±0.9	0.82±0.2
PGF2 α	0.36±0.07	0.55±0.1	1.24±0.5	0.6±0.1
LOX	Treatment Groups			
	Sham	Sham+ TPPU	TAC	TAC+ TPPU
5-HETE	11.2±2.2	8.2±0.5	15.5±1.3	8.4±2
8-HETE	3.4±0.6	1.2±0.6	5.0±1.9	2.1±0.7
11-HETE	2.3±0.3	0.7±0.2	3.8±1.0	2.6±0.5
12-HETE	53.4±10	53.8±2.4	472±161	34.3±12
15-HETE	11.0±1.6	6.7±0.7	12.1±2.3	9.93±1.7

TXB₂; Thromboxane 2, PGF2 α ; Prostaglandin F2 α , COX-2; Cyclooxygenase -2, LOX; Lipoxygenase, HETE; Hydroxyeicosatetraenoic acid